Acta Astronautica 202 (2023) 214–228

Contents lists available at ScienceDirect

Acta Astronautica

journal homepage: www.elsevier.com/locate/actaastro

Research paper

Novel propellant settling strategies for liquid rocket engine restart in microgravity

Á. Romero-Calvo [a,*], Vladislav Urbansky [b], Vadim Yudintsev [b], Hanspeter Schaub [a], Valeriy Trushlyakov [b]

[a] Department of Aerospace Engineering Sciences, University of Colorado Boulder, CO, USA
[b] Aircraft and Rocket Building Department, Omsk State Technical University, pr. Mira 11, 644050 Omsk, Russian Federation

ARTICLE INFO

Keywords:
Liquid rocket
Engine restart
Microgravity
Cryogenics
Magnetic Positive Positioning
Propellant Gasification

ABSTRACT

The active deorbiting and passivation of launch vehicles has become key for the implementation of modern space debris mitigation guidelines. Appropriate engine restart conditions must be provided as part of this process. Ullage motors have been traditionally employed to induce active settling and ensure a gas-free propellant supply to the engines. Although robust and reliable, ullage motors are also heavy, which motivates the study of alternative approaches to the problem. Classic propellant management devices could potentially be employed in this context, but they are hardly applicable to high flow rate cryogenic liquid systems. This paper explores several novel propellant settling strategies that are particularly well suited for cryogenic propellants. In particular, three distinct Magnetic Positive Positioning concepts, a hydrogen-peroxide-based Propellant Gasification System, and a hybrid device that combines both approaches are introduced. The preliminary technical analysis indicates that the successful development of these technologies could lead to mass savings of hundreds of kilograms and economic gains of several hundred thousand dollars per launch.

1. Introduction

The exploration and commercialization of space has led to the increasing contamination of the Low Earth Orbit (LEO) by non-functional man-made objects. Space debris represents a serious safety hazard for current and future satellites due to the risk of in-orbit collisions, and a concern for the general population during uncontrolled re-entry events. The minimization of debris release during normal operations has consequently become a major goal for the international space community [1].

Launch vehicles (LVs) represent more than 42% of the abandoned intact objects in orbit and account for 57% of the abandoned mass [2]. Recent studies have identified the most dangerous elements in an attempt to guide future active debris removal efforts [2–4], resulting in a list that includes 290 second stages of the Soviet/Russian "Cosmos-3M" LV, 7 of which have been considered among the 50 most concerning space debris objects [4], 110 third stages of the Soviet/Russian "Cyclone-3" LV, 54 units of the American first and second stages of the "Delta" LV, as well as 38 third stages of the Chinese "CZ-4" and "CZ-2D" LVs. Further concerns arise due the presence of propellant residuals in the tanks, which account for up to ~3% of the initial fuel mass [5]. During the long stay of a stage in orbit, the remaining fuel evaporates under the influence of solar radiation, which leads to an increased risk of explosion and, therefore, to the generation of space debris [1]. The uncontrolled descent of first LV stages in sensitive drop areas can also lead to environmental pollution caused by the depressurization of toxic fuels, fires in the drop sites, and the contamination of water bodies. This problem is more relevant for Russian LVs like "Soyuz", "Proton", and "Angara", whose drop zones are mostly located on land [6,7].

Modern launch vehicle operations are subject to strict space debris mitigation policies [1]. When graveyard orbits are not attainable, the orbital lifetime is limited and systems are passivated by removing all energy sources. Active deorbiting represents a highly attractive alternative to those strategies, but it is not exempt from risks and technical challenges [8]. Among them, proper engine restart conditions must be provided once the stage is separated from the rest of the vehicle in order to ensure a safe reorbiting or reentry. This decoupling induces strong disturbances on the propellant residuals and leads to highly nonlinear sloshing dynamics, compromising the operation of the engine feed system [9].

Propellant management devices (PMDs) like porous traps [10,11], troughs [12–14], or start baskets [15,16] have been employed to safely restart rocket engines against moderate accelerations (particularly, in upper launcher stages with storable propellants), but these approaches

* Corresponding author.
E-mail address: alvaro.romerocalvo@colorado.edu (Á. Romero-Calvo).

https://doi.org/10.1016/j.actaastro.2022.10.012
Received 14 March 2022; Received in revised form 19 September 2022; Accepted 5 October 2022
Available online 12 October 2022

do not easily apply to cryogenics due to their complex heat transfer mechanisms and low surface tension. In fact, screen channel liquid acquisition devices are the only type of PMD with cryogenic flight heritage [17]. Although significant efforts are being devoted to the design of cryogenic liquid acquisition systems [18], the inertial (or active) settling approach is far more extended. Ullage engines have been traditionally employed during insertion, orbital coast, or on-orbit operations. These independent rockets induce accelerations that can be as weak as 10^{-4} to 10^{-3} m/s^2 and involve solid, mono-propellant, bi-propellant, or cold gas technologies, sometimes fed by vaporized propellant vented from the main tanks [19]. Some examples include the Saturn IV-B's hypergolic liquid bi-propellant Auxiliary Propulsion System (APS) [20,21], the APS at the Centaur upper stage [22], SpaceX's Falcon 9 nitrogen cold gas thrusters for coast attitude control [23], or the two *Sistema Obespecheniya Zapuska* (SOZ) ullage engines of the Blok DM-2 Proton upper stage. This last unit has raised concerns in the space debris community after being responsible for up to 50 on-orbit explosions between 1984 and 2019 [24].

The technical specifications of ullage engines are not usually accessible to the scientific community, which hampers any effort to perform an "external" evaluation of these systems. However, numerous reports from the Apollo era can still be consulted. The two Saturn IV-B APSs were usually fired in three consecutive ullaging burns for a total of ~245 s, consuming ~13.5 kg of propellant (~23.5% of the total propellant mass of each APS) [25]. The dry mass of the APS is unknown to the authors but seems of the order of several hundred kilograms judging by the volume of the system. The dry mass of Saturn IV-B was about 13.5 t. On the other hand, each one of the two SOZ units of the Block DM-2 upper stage had a dry mass of ~106 kg and a total propellant mass of up to 114 kg, while the stage itself weighted 2.1 t. Although determined by the characteristics of the vehicle and its mission profile, the total mass of ullage rocket systems is usually of the order of hundreds of kilograms [26]. With a Falcon 9's launch cost to LEO of ~2700 $/kg [27], an economic penalty per launch and stage of up to ~500.000 USD may be estimated. This value is doubled for GEO orbits, and multiplied by an even larger factor in a Mars mission.

Although ullage engines are a robust and well-established solution to deal with the restart of rocket engines in microgravity conditions, lower mass penalties and/or enhanced reliability may be found in different technical alternatives. In this paper, the boundary conditions of the propellant settling problem are explored in Section 2, while the performance of three Magnetic Positive Positioning (MP^2) strategies [28], an on-board Propellant Gasification System (PGS) [29], and a hybrid device are addressed in Sections 3, 4, and 5, respectively. The historical background of each system is presented together with a preliminary technical analysis. The ultimate goal of this work is to initiate an open discussion on these technologies and inform the design of related propellant settling systems.

2. Launcher characteristics

2.1. Overview

Although applicable to multiple low-gravity propellant settling systems, the discussion that follows focuses on the first and second launch stages of a Falcon-9-like LV. The basic parameters of the vehicle are reported in Table 1, with the geometrical definitions being depicted in Fig. 1. Some of these values are found in SpaceX's Falcon User's Guide [23], while others can only be estimated from unofficial sources.[1]

[1] See www.spacelaunchreport.com/falcon9ft.html Consulted on 13/01/2022.

Table 1
Geometrical and inertial parameters of the launch vehicle.

Parameter	First stage	Second stage
Propellant type	LOX + RP1	LOX + RP1
Empty mass [t]	22	4.5
Propellant mass [t]	411	111.5
Oxygen tank capacity [t]	287.4	78
Kerosene tank capacity [t]	123.5	33.5
Total mass [t]	433	116
Propellant after separation [t]	13	3.5
Propellant after landing [t]	1	0.3
Thrust (stage total) [kN]	7686	981
Throttle capability [kN]	4381 to 7686	626 to 981
Number of engines	9	1
Diameter [m]	3.66	3.66
LOX tank height L_0 [m]	22.5	8.7
Length of 1 stage h_0 [m]	29	11.2
Length of fuel tank h_g [m]	19.2	7.4
First stage mass center x_c [m]	14.9	5.7
Moment of inertia [kg m^2]	$2.68 \cdot 10^6$	$3{\cdot}10^4$
Length to PGS nozzles h_n [m]	39	15

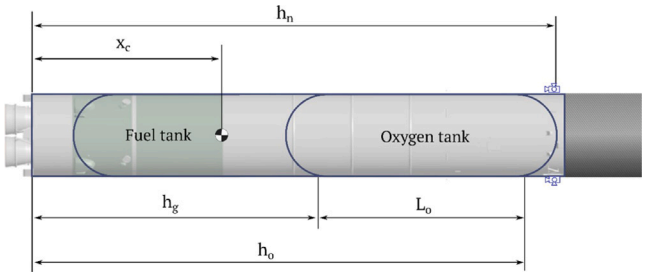

Fig. 1. Geometrical parameters of a launch vehicle stage.

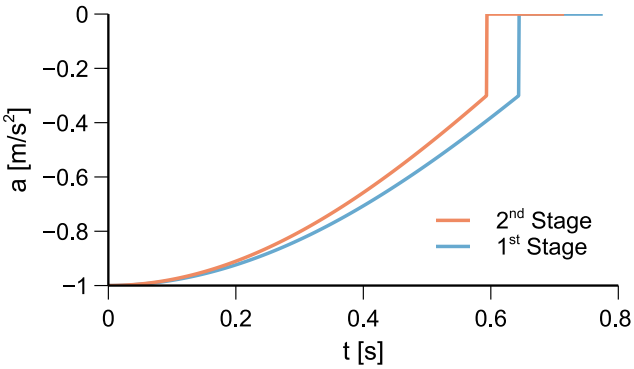

Fig. 2. Estimated acceleration profile of the 1st and 2nd stages after separation.

2.2. Propellant behavior during stage separation

The acceleration profile experienced by each stage during separation is key to understand the dynamic behavior of the propellant. A simple mechanical model is introduced in the Appendix and employed to obtain the acceleration curves reported in Fig. 2 using representative values. Peak accelerations of ~1 m/s^2 are applied to the system and sustained for less than 1 s. Additional effects that may impact the propellant behavior include the release of strain energy from the walls of the tank, the flow movement induced by engine suction, or thermal convection [19].

Modeling this problem is far from trivial, and experimental data is not easily available because of its consideration as Export-Controlled material. However, a partial recording of Falcon 9's first and second stage liquid oxygen (LOX) tanks during the CRS 5 mission is publicly

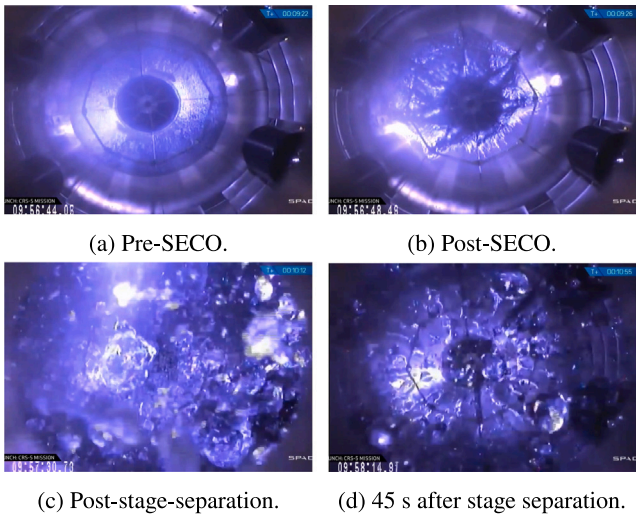

(a) Pre-SECO. (b) Post-SECO.

(c) Post-stage-separation. (d) 45 s after stage separation.

Fig. 3. Top view of the second-stage LOX tank of SpaceX's Falcon 9 during the CRS-5 mission.
Source: www.youtube.com/watch?v=mVAGoWJuDKk.

available,[2] allowing for a qualitative analysis of the problem. Fig. 3 shows the sequence of video frames for (a) the instant before second-stage engine cut off (SECO), (b) the lateral sloshing wave caused by the structural relaxation after SECO, (c) the cloud of LOX bubbles generated after separation, and (d) the state of the cloud 45 s after separation. It can be readily concluded that (i) the SECO induces a mild lateral sloshing wave, but does not significantly disturb the liquid, (ii) the stage separation atomizes the residual LOX in a myriad of droplets that reach the top of the tank in less than 40 s (i.e. the droplets move at least at ~20 cm/s), and (iii) the droplets keep moving for at least 6 min while coalescing with each other. This behavior is also (briefly) observed in the first stage, where the droplets seem to move at about 0.5 m/s. This value has been employed in the derivation of the acceleration profiles shown in Fig. 2.

2.3. Engine restart conditions

The propellant must be settled over the fuel outlet to ensure a safe engine restart. Although this usually implies bringing *all* the liquid back to the bottom of the tank before ignition, the requirement may be instead reformulated by noting that the engines will also accelerate the stage. The goal is thus to have enough propellant at the outlet so that, when the thrust-induced settling brings all the liquid to the bottom of the tank, no gas bubbles have made their way into the engines. This design philosophy is shared by many traditional types of PMDs [17].

The first factor to consider is mass flow rate: higher thrust will settle the propellant droplets faster, but will also require a larger initial mass. The relation between thrust T and mass flow rate $\dot{m}_p$ is given by

$$T = I_{\mathrm{sp}} g_0 \dot{m}_p, \tag{1}$$

where I_{sp} is the specific impulse and $g_0 = 9.81$ m/s^2 is the standard gravity acceleration. For a LOX-RP1 chemical engine with a mass ratio of ~2.3 the specific impulse should be around 285 s at sea level [30]. In fact, SpaceX attributes to Falcon 9's Merlin engines the values of 282 s at sea level and 311 s in vacuum.[3] The second factor is the propellant settling time, that can be divided into two phases. On the first, propellant residuals return to the intake device, while on the second, gas bubbles are removed from the liquid. The total settling time can thus be expressed as

$$t_s = t_I + t_{II}. \tag{2}$$

For a tank of length L, the duration of the first phase is bounded by the kinematic result

$$t_I = \sqrt{\frac{2Lm_0}{T}}, \tag{3}$$

with m_0 being the dry mass of the stage. The duration of the second phase, assuming a constant terminal velocity of the bubbles in the liquid, is [31]

$$t_{II} = l\left[\frac{8}{3}\frac{r_b T}{C_d m_t}\left(1-\frac{\rho_g}{\rho_l}\right)\right]^{-1/2} \tag{4}$$

where r_b is the bubble radius, C_d is the drag coefficient, ρ_g is the gas density, ρ_l is the liquid density, m_t is the total mass of the stage after settling, and l is the height of the longest liquid column. Consequently, the initial mass of propellant required to complete the maneuver for a giving thrust level is

$$m_p = \dot{m}_p t_s = \frac{T}{I_{sp} g_0}\left\{\sqrt{\frac{2Lm_0}{T}} + l\left[\frac{8}{3}\frac{r_b T}{C_d m_t}\left(1-\frac{\rho_g}{\rho_l}\right)\right]^{-1/2}\right\}, \tag{5}$$

which increases with $\sqrt{T}$, showing that small thrust values are convenient to minimize the mass of propellant required to restart the engines. Table 2 reports the stage acceleration, settling time, and initial oxidizer and fuel masses for different thrust configurations of Falcon 9's first and second stages. The values $C_d = 0.47$ (sphere at $Re = 10^3$ to 10^5 [32]), $r_b = 5$ mm, $\rho_g = 0.1785$ kg/m^3 (He), $\rho_l = 1141$ kg/m^3 (LOX), and $l = m_r/(\pi R^2 \rho_l)$, with R being the tank radius and m_r the residual LOX mass, are employed in combination with those presented in Table 1 using the larger LOX tank as a reference. The masses reported in Table 2 are the minimum absolute values required near the fuel outlet to initiate the restart maneuver. Unofficial sources claim that Falcon 9's first stage restart acceleration is less than 50 m/s^2 by employing reverse engineered telemetry data,[4] which indicates that either the central engine at maximum thrust or three outer engines at minimum thrust are actually employed in this process. However, the authors were not able to verify this information.

3. Magnetic Positive Positioning

3.1. Concept and overview

The ability of controlling the position of susceptible liquids by means of magnetic fields leads to several applications in microgravity environments. Those include, but are not limited to, mass transfer [33–36], thermomagnetic convection [37,38], or micropropulsion [39,40]. The magnetic polarization force enables these technologies and is defined by

$$\boldsymbol{f}_m = \mu_0 M \nabla H, \tag{6}$$

with μ_0 being the permeability of free space, and M and H denoting the magnetization and magnetic fields, respectively. In addition, the *magnetic normal traction*

$$p_m = \mu_0 \frac{M_n^2}{2} \tag{7}$$

should be considered at the liquid interface, where M_n is the normal magnetization component [41]. This pressure-like term is usually neglected for *natural* liquids, such as LOX, but becomes relevant for highly

[2] The interested reader is referred to https://youtu.be/p7x-SumbynI. Consulted on 13/01/2022.

[3] See web.archive.org/web/20130501002858/http://www.spacex.com/falcon9.php. Consulted on: 13/01/2022.

[4] See https://github.com/shahar603/SpaceXtract for a remarkable example of reverse engineering. Consulted on 17/01/2022.

Table 2
Stage acceleration, settling time, and minimum initial oxidizer and fuel masses for different restart configurations of Falcon 9's first and second stages.

	First stage				Second stage			
	g[m/s^2]	t_s[s]	LOX[kg]	RP1[kg]	g[m/s^2]	t_s[s]	LOX[kg]	RP1[kg]
Maximum thrust	350	0.66	1287	401	218	0.39	88	38
Minimum thrust	200	0.88	971	303	140	0.49	70	30
Single engine	22	2.63	324	101	140	0.49	70	30

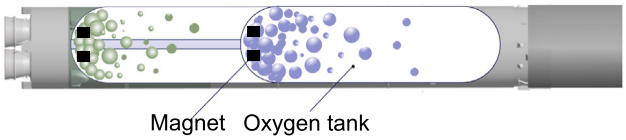

Fig. 4. Magnetic Positive Positioning.

susceptible materials like high-density ferrofluids [42]. Since both H and its gradient decay with the distance to the source, the magnetic force vanishes relatively quickly. Therefore, high-density magnets or powerful coils are needed for most applications.

The MP^2 approach, sketched in Fig. 4 for the system under study, seeks to induce a magnetic acceleration that holds, collects, and/or traps the liquid near the fuel outlets. The concept was first proposed in 1963 by Steve Papell in the same patent where he invented ferrofluids [43]. The idea was abandoned until the late 1990s when, motivated by the advent of stronger permanent magnets and high-temperature superconductors, the NASA Magnetically Actuated Propellant Orientation (MAPO) experiment explored the positioning of ferrofluid solutions in a series of parabolic flights [44]. Such ferrofluids were selected to approximate the magnetization curve of LOX for different magnetic field intensities. It should be noted that LOX is the most susceptible natural paramagnetic liquid [45], making it particularly appropriate for this application. Subsequent publications by Marchetta and coworkers presented refined numerical models and results of technical relevance for the development of liquid oxygen magnetic positioning devices [46–54]. Recent works have also explored the free surface oscillations of ferrofluids in microgravity, which may be relevant for slosh control and the development of novel PMDs [55–60]. A comprehensive review of the field can be found in Ref. [28].

Significant advances have been made in the modeling and fundamental understanding of MP^2 devices during the last two decades. However, none of the aforementioned works explored the feasibility of this approach as part of the operation of LVs. Although constrained by the limited access to technical information, this section aims at covering this knowledge gap by exploring the application of MP^2 to the restart of Falcon 9's first and second stages.

3.2. Passive retention strategy

The first and most intuitive approach to MP^2 is the liquid retention strategy, where a magnet or coil is used to hold the paramagnetic liquid in the presence of adverse accelerations that tend to destabilize the free liquid surface. In the classical literature, the critical Bond number

$$Bo^* = \frac{\rho g^* R^2}{\sigma} \tag{8}$$

is employed to compute the critical acceleration load g^* for which surface tension, with coefficient σ, cannot longer stabilize the meniscus. Myshkis and coworkers provide a best-case $Bo^* = -3.32$ for cylindrical tanks at a contact angle of 90° [61], which results in $g^* = 2.9 \cdot 10^{-6}$ m/s^2 for the LOX tank considered in this work. In other words, surface tension does little or nothing to prevent the atomization of the residual LOX volume observed in Fig. 3 under the action of the acceleration loads estimated in Fig. 2. A logical follow-up questions is whether the magnetic force can hold the liquid against adverse accelerations of ~1 m/s^2.

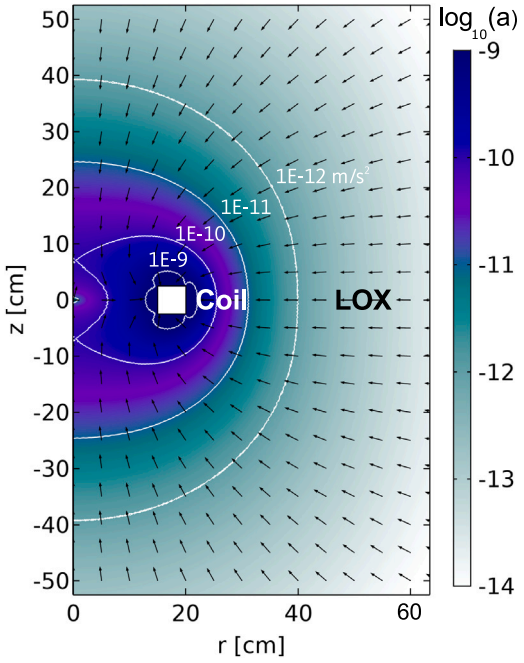

Fig. 5. Magnetic acceleration contours induced on LOX by a 35 cm diameter coil operating at 1 At.

Marchetta and coworkers explore the problem of magnetic LOX retention in a 12 cm diameter 24 cm height cylindrical tank under the influence of a point dipole of 1.4 cm diameter and an inertial acceleration along its major axis [53]. The dipole strength required to hold ~30 ml of liquid is shown to be about 10 Am^2 for $g^* = 1$ m/s^2. Similarly, in Ref. [28] an analytical model is developed to study the stability of magnetic interfaces and applied to a 10 cm diameter cylindrical tank, showing that a 60 g magnet can increase the critical load by 31.5%. None of these low-gravity studies can be easily extended to Falcon 9's 3.66 m diameter LOX tank, where the liquid outlet has a diameter of about 90 cm and the maximum estimated acceleration is about 1 m/s^2. The problem, however, can be easily addressed by plotting the axisymmetric magnetic acceleration contours induced by a 1 A cylindrical coil on the LOX tank volume as done in Fig. 5. The figure depicts the magnetic acceleration levels in a logarithmic scale and its direction using black arrows. A coil mean diameter of 35 cm is chosen to ensure that the liquid gets attracted toward the PMD located at the tank outlet. The minimum mass to be retained is 70 kg (second stage), which translates to a LOX sphere of 25 cm radius. The magnetic acceleration at this distance is about 10^{-11} m/s^2. Since the acceleration scales with the square of the current intensity [28], values of ~10^6 At (i.e. coils current intensity times number of coil turns) would be required to retain the oxidizer against accelerations of 1 to 10 m/s^2. Further computations are not required to conclude that the mass and/or power requirements of this approach are well beyond reason with existing technologies, particularly for the first stage.

3.3. Recovery strategy

The passive magnetic retention strategy sets an upper limit for the magnetic field strength. Because this limit is practically impossible to reach, alternative strategies must be explored. To the best knowledge of the authors, none of them has been proposed before and are therefore characterized by very low Technology Readiness Levels (TRLs). The first of them is here introduced and seeks to collect the LOX droplets after they are atomized rather than holding part of the liquid at the bottom of the tank. In order to evaluate this idea, the time required to settle a LOX droplet is first derived with a simplified framework of analysis.

3.3.1. Magnetic settling time

If the settling of the propellant is induced by the magnetic interaction and not by a uniform acceleration g, the derivation of t_s is complicated by the presence of an inhomogeneous acceleration field. A strict approach to the problem would require solving the Navier–Stokes equations with a magnetic force source term. Although less computationally expensive than the fully coupled fluid-magnetic simulations that are necessary for highly susceptible ferrofluids [28], this approach is still prohibitive for a preliminary study. Instead, the movement of a perfectly spherical droplet along the symmetry axis of an axisymmetric coil or magnet is analyzed. The droplet is small in comparison with the variation of the magnetic field and exhibits linear magnetization with susceptibility $\chi \ll 1$. It is further assumed that external, internal, and magnetization fields are collinear, that residual liquid volumes do not contribute to the magnetic field, and that magnetic surface force terms are negligible. In this simplified framework, the total magnetic force induced on the liquid droplet by a circular coil with n turns, radius R, and current intensity I at a distance z along the symmetry axis $\boldsymbol{e}_z$ is[5]

$$\boldsymbol{F}_m \approx -\frac{3\mu_0\chi(nI)^2R^4}{4}\frac{z}{(R^2+z^2)^4}\boldsymbol{e}_z. \tag{9}$$

This expression can also be applied to axially magnetized cylindrical magnets with magnetization M_m, radius R and height l_m by considering an equivalent circular coil with the same radius and current intensity $nI = M_m l_m$. Its main advantage is that it allows the derivation of a quasi-analytical expression for t_I. After considering Newton's second law and solving the resulting second-order differential equation with initial position $z(0) = L$ and velocity $\dot{z}(0) = 0$, the duration of the first phase becomes

$$t_I(L) = \sqrt{\frac{4\pi\rho_l}{\mu_0\chi(nI)^2R^4}} \cdot \int_0^L \left[\frac{1}{(z^2+R^2)^3} - \frac{1}{(L^2+R^2)^3}\right]^{-1/2} dz, \tag{10}$$

where it should be noted that t_I is inversely proportional to nI (or, if a magnet is employed, to $M_m l_m$) and R^2. Of these, only the current intensity can be considered a design parameter because R is bounded by the fuel intake radius (see Section 3.2).

The time required to debubble the multiphase mixture near the fuel outlet using the paramagnetic force can be derived in a similar way [63]. However, the magnetic debubbling process is much faster than the droplet settling phase because the liquid is closer to the magnetic source, and hence it is further assumed that $t_s \approx t_I$. Even though the assumptions employed in the derivation of Eq. (9) are not appropriate for highly susceptible ferrofluids, the volume magnetic susceptibility of the liquids employed in this work is bounded by that of LOX ($\chi_{\mathrm{LOX}} = 0.0034$ at 90 K and 1 atm [45]). It would not be particularly useful to employ high density ferrofluids in the fuel tank when the most demanding requirements are associated with the LOX tank.

[5] Eq. (9) can also be found in the literature divided by the term $(1+\chi)^2$ or $(1+D\chi)^2$, with $D = 1/3$ being the demagnetization factor of a sphere [28,42,62]. Each choice denotes a different modeling of the internal magnetic field inside the droplet. Since in the problem here considered $\chi \ll 1$, the simplest approach, that assumes $H_0 \approx H$, is adopted.

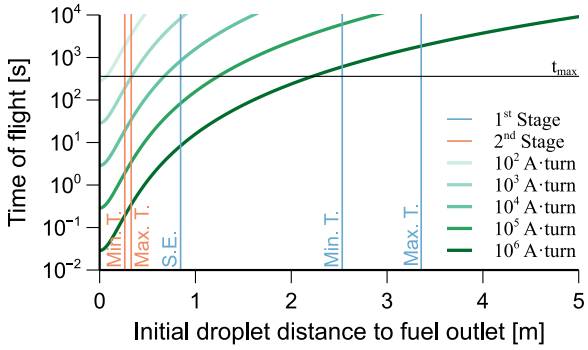

Fig. 6. Time required by a LOX droplet to reach the bottom of the tank as a function of its distance to the coil and the applied current intensity. The minimum tank settling length required by the single engine (S.E.), minimum thrust (Min. T.) and maximum thrust (Max. T.) configurations is superposed.

3.3.2. Performance analysis

The time of flight of the droplets for a coil diameter of 35 cm is represented in Fig. 6 as a function of the initial droplet distance to the coil and the applied current intensity. A LOX settling time of $t_{\max} \approx 6$ min, estimated in Section 2, is superposed and treated as a deadline for the collection process. However, unofficial telemetry data shows that the first stage restarts 2 to 3 min after stage separation (see footnote 4). As it will be seen, this does not change the qualitative results of the analysis. It is arbitrarily assumed that, after atomization, the LOX droplets are uniformly distributed in the tank volume. In this framework, the vertical lines represent the tank length that needs to be settled for each one of the configurations detailed in Table 2 before the LOX droplets stop moving (i.e. get attached to the walls of the tank).

A qualitative difference is first observed between first and second stages. The LOX mass required to restart the engines, listed in Table 2, drops by an order of magnitude in the second stage, and thus a smaller tank length needs to be settled. The second factor that should be considered is the density of residual LOX per unit tank length. Although the lower LOX tank is 22.5 m and the upper is just 8.7 m, the density of residual LOX is relatively similar, decreasing from 383.5 kg/m to 267 kg/m, respectively. Fig. 6 shows that a coil with a configuration of 10^3 A·turn can satisfy the requirements of the second stage. However, 10^4 to 10^5 A·turn are needed to settle the first stage using the single engine restart configuration, with 10^6 to 10^7 A·turn being required for the rest. In other words, the liquid recovery strategy can potentially reduce the coil strength requirements by one order of magnitude in the first stage and three orders of magnitude in the second. These conclusions do not change if $t_{\max}$ drops to 120–180 s for the first stage, as indicated by unofficial telemetry data.

These results should be taken with care due to the number of assumptions employed in the derivation of Eq. (10). In particular, fluid–structure interactions have been completely ignored, but Fig. 3 shows that, after a few minutes, the liquid droplets tend to get stuck to the walls of the tank. This is a natural consequence of the presence of wetting surfaces and corner geometries in the interface between PMDs and the walls. The robustness of the liquid recovery strategy may thus be compromised by this effect, which should be evaluated with flight data that is not available to the authors. Possible mitigation strategies include the elimination of gaps and corner geometries or the application of a LOX-phobic treatment to the internal surfaces.

3.3.3. Liquid lines

The discussion provided in this section focuses on attracting the propellant residuals to the bottom of the tank after stage separation. However, for the system to effectively prevent the ingestion of gas bubbles, conduits connecting the propellant tank to the engines must remain filled with liquid during the whole process. Start baskets, traps,

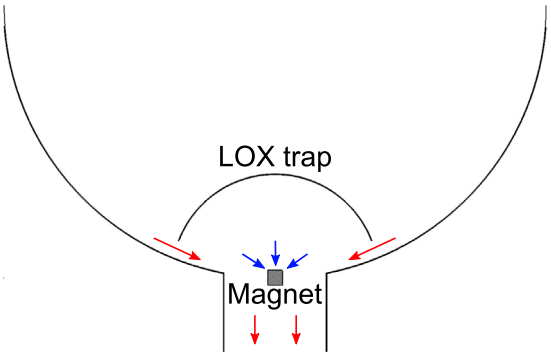

Fig. 7. Conceptual magnetic trap system for Falcon 9's first stage LOX tank. Red and blue arrows indicate the propellant flux in hyper- and microgravity conditions, respectively. (For interpretation of the references to color in this figure legend, the reader is referred to the web version of this article.)

or troughs, whose characteristics and historical heritage are thoroughly described in Ref. [17], may be employed to instantaneously hold the liquid against accelerations of ~1 m/s^2. Retaining the minimum masses computed in Table 2 while enabling high cryogenic mass flow rates is far from simple, and it is in this context where the magnet can help reduce the volume of the trap by ensuring that part of the propellant is collected after stage separation.

The employment of cryogenic propellants may lead to additional gas trapping issues in the liquid lines between stage separation and engine restart. For instance, LOX could start boiling over hot surfaces. The relevance and impact of these events depends on environmental factors that are unknown to the authors but that must be considered by the designer.

3.4. Magnetic trap

As previously noted, capillary PMDs are far less effective in ensuring the safe restart of cryogenic engines in comparison with storable liquids due the low surface tension of the propellant [17]. Furthermore, the presence of meshes or screens can severely increase the pressure drop across PMDs in high flow rate tank outlets, rendering this approach unfeasible for launch vehicles. The magnetic trap system here proposed faces these issues by combining a screen-less clam shell trap aimed at holding the liquid and a magnet employed to induce reorientation in microgravity.

Fig. 7 depicts a conceptual magnetic trap for Falcon 9's first stage LOX tank. When the engine is in operation, the flux of LOX surrounds the trap and reaches the fuel outlet. Because inertia is dominant, the magnetic force has a marginal effect on the flow. Stage separation triggers the unfavorable acceleration profile estimated in Fig. 2 and part of the liquid escapes the trap. The volume of released propellant and the risk of gas injection depend on the geometry of the system and should be quantified numerically. Once the launcher reaches microgravity conditions, the magnet located at the fuel outlet reorients the remaining liquid oxygen and prevents the ingestion of gas bubbles. The trap can be refilled by installing a vent tube on top of the structure [11]. It is important to highlight that, unlike similar capillary systems, the magnetic trap does not prevent the ingestion of gas bubbles in the trap space; instead, it ensures that the required volume of gas-free propellant reaches the fuel outlet by employing a localized magnetic polarization force.

The magnetic acceleration field on LOX of a 5 cm radius, 10 cm height cylindrical magnet magnetized at 1300 kA/m is shown in Fig. 8. The geometry differs from that of Fig. 5 in the adoption of a smaller radius, which increases the magnetic force close to the source [28] and makes this configuration more suitable for magnetic traps. The magnet

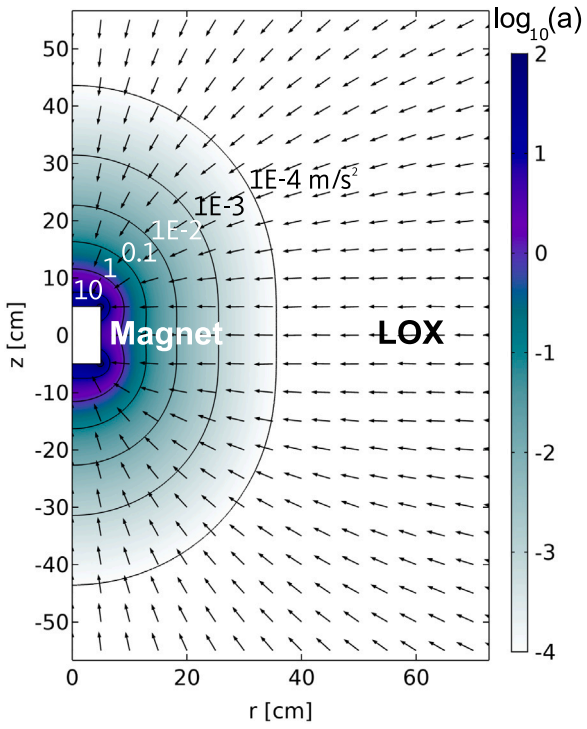

Fig. 8. Magnetic acceleration field induced by a 5 cm radius 10 cm height praseodymium magnet magnetized at 1300 kA/m.

volume is chosen to impose an acceleration of 10^{-4} m/s^2 (one order of magnitude larger than microgravity disturbances [19]) at ~40 cm from the magnet. This leads to the approximate LOX volume that needs to be retained in the single-engine first stage scenario reported in Table 2. Although the mass of the magnet is just ~5.5 kg, the total mass would be close to 20 kg after considering ancillary components like the 2.5 mm aluminum LOX trap wall or its supports.

The same system can be applied to the second stage and would require a 25 cm radius LOX volume with a magnet of just 0.5 kg. The mass of the trap would account for ~2.2 kg. That is, the magnetic trap may potentially achieve mass savings of one to two orders of magnitude with respect to current ullage engine approaches.

3.5. Magnetic field generation

With the nI parameter already sized for the different engine restart configurations, the next logical step is to determine how to produce the required magnetic fields. Three technologies are considered: copper and aluminum coils, rare earth permanent magnets, and superconducting coils.

The magnetic field generated by a coil is linearly dependent on the nI parameter, that can be increased by adding more wire turns or employing higher currents. Total coil mass and power dissipation are the driving factors of the design. The mass of the coil can be estimated as

$$m = 2\pi RnS\rho_w, \tag{11}$$

where S is the cross-section of the wire and ρ_w its density. The heat dissipated by the coil can be derived from Ohm's law, resulting in

$$P = 2\pi RIn\rho_e \frac{I}{S}, \tag{12}$$

with ρ_e being the resistivity of the material. In a worst-case scenario this heat is stored in the coil instead of being dissipated, causing a

Table 3
Mass and power budget for different magnetic configurations.

Current · Turns[At]	Aluminum coil[a]					Praseodymium magnet[b]	
	I[A]	P[W]	n[# turns]	d[mm]	m[kg]	h[mm]	m[kg]
10^2	$2.51{\cdot}10^{-3}$	0.06	4	$1.62{\cdot}10^{-1}$	2.44	0.08	0.052
10^3	$2.51{\cdot}10^{-2}$	0.60	40	$5.12{\cdot}10^{-1}$	24.4	0.77	0.52
10^4	$2.51{\cdot}10^{-1}$	6.03	405	1.62	244	7.7	5.2
10^5	2.51	60.26	4054	5.12	2438	77	52
10^6	24.67	592	40 541	16.2	24 814	769	519

[a]Coil of 35 cm diameter operating at 24 V and 90 K.
[b]Cylindrical magnet of 35 cm diameter magnetized at 1300 kA/m at 90 K.

temperature increase of

$$\Delta T = \frac{P t_{\max}}{m C_p} = \frac{\rho_e t_{\max}}{\rho_s C_p} \left(\frac{I}{S}\right)^2, \tag{13}$$

where C_p is the heat capacity of the wire. In order to constrain the design, the heat dissipated by the coil is limited by considering two worst-case scenarios: in the first, the heat is fully transferred to the residual LOX. The maximum power is arbitrarily set to the one that vaporizes 1 kg of LOX during the 6 min operation of the coils. The latent heat of vaporization of LOX is 6.82 kJ/mol (or 213.13 kJ/kg) at atmospheric pressure [45], which results in a maximum coil power of 592 W. Because nI is fixed, the ratio I/S is determined by Eq. (12). In the second scenario, the heat is stored in the coil, causing a temperature increase that is arbitrarily limited to 10 K. Therefore, the I/S parameter is extracted from Eq. (13). The most restrictive constraint is chosen for each design so that the thermal runaway of the material and the vaporization of the residual LOX volume are avoided. Then, the mass is computed for the I/S value from Eq. (11). The second requirement concerns the voltage of the coil, set to 24 V to ease integration with Falcon 9's power subsystem. After inserting the I/S value in Eq. (12) and employing Ohm's law, the current intensity of the coil and its resistance are computed. At the boiling temperature of LOX (90 K) the resisitivities of copper and aluminum are $3.5{\cdot}10^{-9}$ Ω m and $4.5{\cdot}10^{-9}$ Ω m, respectively [64]. Although copper is slightly more conductive than aluminum, its density and heat capacity are 8960 kg/m^3 and 0.385 kJ/kg K, while aluminum has a density of 2700 kg/m^3 and a heat capacity of 0.89 kJ/kg K. Therefore, aluminum is chosen to minimize the mass of the design.

The second approach focuses on employing rare earth permanent magnets to generate a constant, unpowered magnetic field. Neodymium ($Nd_2Fe_{14}B$) is the most popular rare earth material, has a density of 7008 kg/m^3 [45], and exhibits a remanent magnetization of $M_m \approx 1200$ kA/m. It is classified as a "hard material", implying that it can be used to manufacture magnets of any shape [65]. As previously noted, the sizing parameter nI of a cylindrical coil can be translated to the length l_m of an equivalent cylindrical magnet with the same diameter by means of the expression $In = M_m l_m$. Magnet tessellation strategies such as Halbach arrays can be employed to boost the paramagnetic force on one side, while partially canceling it on the other [66]. Halbach arrays have already been proposed for space applications [63] and would be particularly well suited to the LOX settling problem for two reasons: the reach of the magnet is increased, and the interaction between the LOX magnet and the droplets generated in the fuel tank is reduced.

Neodymium magnets experience a slight increase of their magnetic flux as temperature decreases. At around 135 K, a transition point is reached and the magnet undergoes spin reorientation (i.e. a change in the preferred direction of the magnetization vector) that decreases the flux by no more than a 14%. This process is reverted as soon as the temperature increases [67]. If needed, the transition point could be avoided by isolating the magnet in the LOX tank and actively controlling its temperature. A more elegant solution is, however, to employ praseodymium magnets to avoid the spin reorientation. Praseodymium magnets have been shown to reach a remanent magnetization of ∼1300 kA/m at 85 K [68,69], which makes them ideal for LOX control applications.

The design points of the aluminum coil and praseodymium magnet are shown in Table 3 as a function of the nI parameter. In all cases but 10^6 At, the design of the coil is driven by the thermal requirement (maximum temperature increase of 10 K). Magnets are orders of magnitude lighter for all nI values, incurring in a – still reasonable– mass penalty of 52 kg at 10^5 At. nI values beyond 10^5 At seem unreachable without incurring in large mass penalties, and it is in this context where high-temperature superconductors (HTC) can become a game-changing alternative. A HTC wire exhibits zero resistance in a certain operational range, resulting in no heat loss and a potential reduction in mass and power requirements. This happens when (i) it is operated below its critical temperature T_c –greater, by definition, than the boiling point of nitrogen (77 K)–, (ii) it is subjected to a magnetic field below the critical field B_c, and (iii) the critical current I_c is not exceeded. The simultaneous satisfaction of these three requirements is far from trivial; in fact, I_c decreases continuously with increasing temperature and magnetic field [70]. For example, Bi2223 ($Bi_2Sr_2Ca_2Cu_3O_{10+\delta}$) has a critical temperature of 110 K, but its critical current drops to zero when the material is exposed to a field of less than 1 T. RE-123 ((RE)$Ba_2Cu_3O_7$, where RE stands for Rare Earth element) superconductors (also known as REBCO), on the contrary, can resist up to 10 T, but only well below a critical temperature of around 90 K [71]. It is nowadays feasible to generate very strong magnetic fields at the boiling point of Helium (4.22 K), a good example being the 32 T superconducting magnet [72] of the National High Magnetic Field Laboratory.[6] Reaching similar values at higher temperatures still seems, unfortunately, beyond our technical capabilities. In the application here discussed the superconductor would be immersed in LOX, which would act as a cooling agent only if $T_c \gg 90$ K, and the maximum magnetic field imposed near the coils would be ∼10 T at $In = 10^6$ At. The results presented in Ref. [70] for different commercial REBCO conductors seem to indicate that such operation point cannot be reached with current technologies. However, the I_c value of 4 mm wide superconductors is shown to be 450–1000 A/mm at 12 T and 77 K, a value that jumps up to 60 kA/mm^2 at 18 T and 4.2 K. This indicates that cooling mechanisms need to be put in place to reach the 10^6 At configuration with HTCs, which may open an opportunity for multiple-use of the helium tanks employed for tank pressurization. This possibility, although attractive, would require a deeper technical analysis that is beyond the scope of this paper.

The coils and magnets listed in Table 3 not only induce magnetic polarization forces on the liquid but also on the surrounding structure. However, the magnetic susceptibility of most aerospace alloys is at least two orders of magnitude smaller than that of liquid oxygen, leading to very weak magnetic forces (e.g. aluminum is a paramagnetic material with $\chi_{Al} \approx 2.2 \cdot 10^{-6}$). Although ferromagnetic materials do experience strong forces in the presence of magnetic fields, their use in aerospace systems is generally very limited due to their high density. The (rare) incompatibilities arising during the design should be addressed on a case-by-case basis. Interactions with electrical equipment are negligible in most conceivable scenarios due to the steady nature of the

[6] See https://nationalmaglab.org/magnet-development/magnet-science-technology/magnet-projects/32-tesla-scm. Consulted on: 26/12/2021.

magnetic field employed to position the liquid. Furthermore, electrical problems have not been observed in previous magnetic liquid sloshing experiments [57].

3.6. Fuel tank

From the magnetic actuation perspective, LOX determines the design envelope of the system. On one hand, the LOX tank is more than two times larger than the fuel tank, and therefore a given magnetic source will reach a larger portion of the latter. On the other, LOX is a paramagnetic substance with volume magnetic susceptibility $\chi_{\mathrm{LOX}} = 0.0034$ [45], while kerosene is a diamagnetic with $\chi_{\mathrm{Ke}} \approx -8 \cdot 10^{-6}$ [73]. In order to apply the same MP^2 strategies to the fuel tank, it must be transformed into a para/ferromagnetic by adding magnetic nanoparticles and creating a kerosene-based ferrofluid. With this approach, the susceptibility of the solution is bounded by the concentration of magnetic nanoparticles.

The use of metal-based particles in liquid propellants has been analyzed since the 1950s with the goal of enhancing ideal propulsion performances [74]. Kerosene has been employed as a carrier liquid for ferrofluids since their invention in 1963 [43] and kerosene-based ferrofluids are synthesized and used in numerous fields [75–78]. Commercial solutions like Ferrotec's EMG-905[7] are now widely available at a relatively low cost. The initial susceptibility of a monodisperse, colloidal ferrofluid can be estimated as [41]

$$\chi_{\mathrm{ini}} = 8\phi\lambda, \tag{14}$$

where ϕ is the volume fraction of magnetic solids and λ is the coupling coefficient, given by

$$\lambda = \frac{\mu_0 M_d^2 V}{24kT}, \tag{15}$$

with M_d being the saturation moment of the bulk magnetic solid, V the nanoparticle volume, k the Boltzmann constant, and T the absolute temperature. Assuming an iron oxide nanoparticle radius of 5 nm, an absolute temperature of 293 K, and a saturation moment of 446 kA/m [79], the approximate volume fraction required to match the magnetic susceptibility of LOX starting from the value of kerosene would be just $\phi \approx 3.2 \cdot 10^{-4}$. Not surprisingly, this value is within the range tested by Martin and Holt in the NASA MAPO experiment [44].

If the whole kerosene tank volume is magnetized, the magnetic nanoparticles add ∼40 kg and ∼11 kg to the first and second stages, respectively, in addition to negligible variations in density and specific impulse [28]. The very low ferrofluid concentration should prevent damage to the engines. Although simple, this approach is expensive and inefficient. A better alternative is to enhance only the volume of kerosene employed to restart the engine by adding a concentrated ferrofluid volume shortly before Main/Second Engine Cut-Off (MECO/SECO). The mass penalty associated with the addition of nanoparticles would be of just 40 to 140 g based on the values presented in Table 2.

4. Propellant Gasification System

4.1. Concept and overview

The injection of hot gases into the tanks for chemical pressurization through propellant evaporation and combustion has long been known and used in the "Proton", "Rokot" and "Dnepr" launch vehicles [80]. These systems do not require heat exchangers, which are used to heat cold helium gas from 90 K to 300 K in current pressurization systems, and are instead based on feeding a nitric acid–based oxidizer and fuel into the fuel and oxidizer tanks, respectively. The components ignite and heat is released, causing the fuel to vaporize, which increases the pressure in the tanks. Referring to Sutton [30], while this type of pressurization system is small and lightweight, it has generally not yielded reproducible tank pressures due to the difficulties to stabilize the combustion reaction. For instance, fuel sloshing caused by vehicle maneuvers results in sudden cooling of the hot pressurizing gas and leads to erratic tank pressure changes. This problem can be avoided by physically separating the hot gas from the liquid propellant. If the hot gas is generated from a solid propellant reaction or from mono-propellant decomposition instead of a high-pressure gas supply, a significant reduction in the mass of the pressurizing system can be achieved.

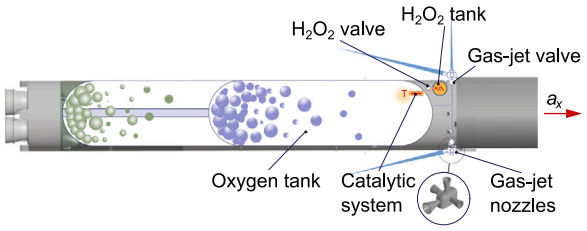

Fig. 9. Propellant Gasification System.

The Propellant Gasification System concept was first proposed in the early 2010s as a method to vaporize the propellant residual of 2nd launch vehicle stages and provide attitude and orbit control capabilities by means of dedicated vapor-fed thrusters [81–83]. The original idea was to inject the combustion products of two-component propellants (nitrogen tetroxide – NT – and nonsymmetrical dimethylhydrazine – NDMH –) in the tank to move the stage from its initial circular orbit to an elliptical orbit. Such orbit would ensure a successful deorbiting in the time frame of 25 years. In 2015, the use of solid fuel instead of a two-component propellant was investigated to simplify the design and improve the energy performance of the PGS. Further analyses on the Soyuz 2.1v launch vehicle showed that the PGS could also lead to launch vehicle characteristic speed enhancements of up to 5% [84]. The PGS baseline design has currently evolved to reduce its mass and environmental impact using a green mono-propellant (hydrogen peroxide) that adds the possibilities of (i) controlling the movement of the stage to reach a given drop area, (ii) providing conditions for LRE restart by executing the flip around and propellant settling maneuvers, and (iii) passivating the propellant after a normal or emergency cutoff of the LRE [85]. Highly concentrated hydrogen peroxide (85%) has already been employed as a green mono-propellant in substitution of hydrazine on the "Soyuz" launch vehicle for the operation of turbo-pump units [86].

The PGS considered in this work vaporizes the propellant residuals in the oxidizer tank of the launch vehicle using the catalytic decomposition of hydrogen peroxide, which is placed in an auxiliary tank and used as a heat source. The mono-propellant is passed through a catalyst chamber that leads to the formation of up to 823 K hot oxygen and steam. The vapor–gas mixture is then transferred into the oxidizer tank, which leads to vaporization of the liquid phase and a pressure increase. The gas, consisting of vaporized propellant and pressurizing agent (helium), is used to feed a set of gas thrusters that are employed for attitude control and tank settling, as sketched in Fig. 9. This approach can be regarded as the active equivalent of the hydrogen venting strategy employed in the Apollo era [19].

It is important to remark that the risk of combustion or explosion is virtually non-existent in the proposed PGS approach. Since only hot hydrogen peroxide decomposition byproducts (water vapor and oxygen) are injected into the oxidizer tank and a reducing agent at auto-ignition temperatures is not present, the combustion reaction cannot be produced. Such a hazard could only occur if the PGS was used in

[7] See https://ferrofluid.ferrotec.com/products/ferrofluid-emg/oil/emg-905/. Consulted on: 28/12/2021.

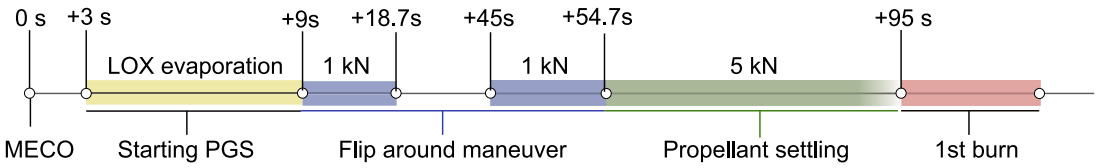

Fig. 10. PGS Concept of Operations.

the fuel tank. However, this approach has already been applied to the aforementioned chemical pressurization systems, and the reaction was safely controlled by tuning the pressurizer gas flow rate.

The following main subsystems compose the PGS: (i) a hot gas generator that includes a bladder-controlled hydrogen peroxide tank and a catalyst chamber where the exothermic decomposition of hydrogen peroxide happens, producing a high-temperature vapor–gas mixture (VGM) with a 34% H_2O and 66% O_2 composition, (ii) a system of nozzles installed after the catalyst chamber that injects the VGM into the LOX tank minimizing tank wall heating, and (iii) a system of gas nozzles used to discharge the VGM from the tank and produce the required thrust. The PGS provides control over the tank discharge valves, hydrogen peroxide feeding, and gas nozzles. Cold helium gas, which is stored in balloons at the bottom of the oxidizer tank, can also be used to reduce the temperature of the VGM (see next section).

4.2. Concept of Operations

Fig. 10 shows the Concept of Operations for the PGS approach. Three seconds after MECO, the first stage separates from the second stage using a pneumatic pusher (or equivalent). The control system of the 1st stage starts the PGS to increase the pressure in the oxygen tank. Nine seconds after MECO, the PGS opens the attitude control nozzles with a total thrust of 1 kN to start the flip around maneuver, which involves an acceleration phase, a constant angular velocity phase, and a deceleration phase. About 55 s after MECO, a set of nozzles provide 5 kN of axial acceleration before engine re-start.

The PGS can be operated in three distinct modes in combination with the helium pressurization system:

1. Standalone PGS operation: In this case, the main task of the PGS is to vaporize the liquid residuals. The highest gas temperature is employed (823 K).
2. Alternate operation: The residual cold helium pressurizer gas (90 K) is fed into the tank in order to reduce the VGM temperature. This reduces or stops the evaporation of liquid propellant and ensures that the proper quantity of liquid is vaporized to operate the gas thrusters.
3. Combined operation: In this case, the VGM does not vaporize the propellant residuals, acting instead as a heat exchanger that warms up the pressurizer gas up to an accepted operational temperature (300 K), replacing the engine heat exchanger [87].

4.3. Flip around maneuver

The flip around maneuver to the required $\Delta\phi$ angle consists of three phases that are evaluated in Fig. 11. The acceleration phase is produced with constant angular acceleration ϵ until the speed ω is reached, and lasts

$$t_\epsilon = \frac{\omega}{\epsilon}, \tag{16}$$

where zero initial speed and angle are assumed. The second phase is produced with constant angular velocity ω and duration t_ω. Finally, the deceleration phase happens with the same angular deceleration. The total turnaround time t_r is given by

$$t_r = \frac{\omega}{\epsilon} + \frac{\Delta\psi}{\omega}. \tag{17}$$

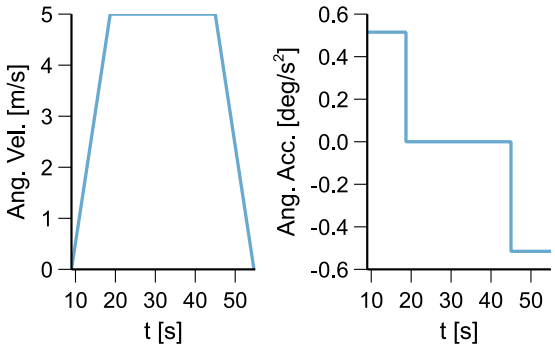

Fig. 11. Angular velocity and angular acceleration profiles of the 1st stage during flip around maneuver using the attitude control nozzles with a total thrust of 1 kN.

Table 4
Parameters of the flip around maneuver.

Parameter	Value
Angular velocity, ω [deg/s]	5
Total attitude nozzle thrust force, F [N]	1000
Acceleration and deceleration phases, t_ϵ [s]	9.7+9.7
Constant angular velocity phase, t_ω [s]	26.3
Total flip around time, t_r [s]	54.7

The magnitude of angular acceleration ϵ is determined by the torque produced by the attitude control nozzles relative to the center of mass and by the lateral moment of inertia of the stage. For instance, around the z-axis the acceleration becomes

$$\epsilon = \frac{F(h_n - x_c)}{J_z}, \tag{18}$$

with F being the total thrust of the nozzles, $h_n - x_c$ the thrust arm, and x_c the distance from the bottom section of the stage to the center of mass. The parameters of the flip around maneuver are given in Table 4.

4.4. Oxygen vaporization model

Vaporization in a tank can occur according to three mechanisms: evaporation without boiling, film boiling, and nucleate boiling. The criterion that determines whether vaporization belongs to one of three types is the temperature of the liquid. The mass rate of vaporization during bubble and film boiling is calculated following a thermodynamic approach that assumes that all the heat supplied is employed to vaporize the liquid.

The mathematical model of the oxygen vaporization process is based on the first law of thermodynamics, and leads to [85]

$$\frac{\mathrm{d}p}{\mathrm{d}t} = \frac{k-1}{V}\left(H_u\dot{m}_{\mathrm{hc}} + i_{\mathrm{hc}}\dot{m}_{\mathrm{hc}} + i_{\mathrm{ev}}\dot{m}_{\mathrm{ev}} - i_{\mathrm{out}}\dot{m}_{\mathrm{out}} - \frac{k}{k-1}p\frac{dV}{dt}\right), \tag{19a}$$

$$\frac{\mathrm{d}\rho}{\mathrm{d}t} = \frac{1}{V}\left(\dot{m}_{\mathrm{hc}} + \dot{m}_{\mathrm{ev}} - \dot{m}_{\mathrm{out}} - \rho\frac{dV}{dt}\right), \tag{19b}$$

$$\frac{\mathrm{d}T_w}{\mathrm{d}t} = \frac{q_{\mathrm{rad}}^{\text{mix-w}} + q_{\mathrm{con}}^{\text{mix-w}} + q_{\mathrm{rad}}^{\text{w-lox}} + q_{\mathrm{con}}^{\text{w-lox}} - q_{\mathrm{rad}}^{w} + q_{\mathrm{ext}}}{c_w m_w} \tag{19c}$$

$$\frac{\mathrm{d}T_{\mathrm{mix}}}{\mathrm{d}t} = \frac{-q_{\mathrm{con}}^{\text{mix-w}} - q_{\mathrm{rad}}^{\text{mix-w}} + q_{\mathrm{rad}}^{\text{w-lox}} + q_{\mathrm{con}}^{\text{mix-lox}} - q_{\mathrm{ev}} + H_u\dot{m}_{\mathrm{hc}}}{c_{\mathrm{mix}} m_{\mathrm{mix}}}, \tag{19d}$$

$$\frac{\mathrm{d}T_{\mathrm{lox}}}{\mathrm{d}t} = \frac{q_{\mathrm{rad}}^{\mathrm{mix\text{-}lox}} - q_{\mathrm{con}}^{\mathrm{mix\text{-}lox}} + q_{\mathrm{rad}}^{\mathrm{w\text{-}lox}} + q_{\mathrm{con}}^{\mathrm{w\text{-}lox}} - q_{\mathrm{ev}}}{c_{\mathrm{lox}} m_{\mathrm{lox}}}. \tag{19e}$$

The system given by Eqs. (19a)–(19e) describes the change of the pressure in the tank p, density of the vapor–gas mixture ρ, and the temperatures of the vapor–gas mixture T_{mix}, LOX T_{lox}, and tank walls T_w. The temperature of the vapor–gas mixture depends on the radiative and convective heat flux to the wall of the tank ($q_{\mathrm{con}}^{\mathrm{mix\text{-}w}}$, $q_{\mathrm{rad}}^{\mathrm{mix\text{-}w}}$), radiative and convective heat flux to LOX ($q_{\mathrm{rad}}^{\mathrm{w\text{-}lox}}$, $q_{\mathrm{con}}^{\mathrm{mix\text{-}lox}}$), heat of vaporization of LOX q_{ev}, and the heat generated during decomposition reaction of H_2O_2 with mass of m_{hc}, $H_u \dot{m}_{\mathrm{hc}}$. The temperature of the walls of the tank depends on the external heat flux from the atmospheric heating q_{ext}, heat flux from the vapor–gas mixture in the tank $q_{\mathrm{rad}}^{\mathrm{mix\text{-}w}}$ and $q_{\mathrm{con}}^{\mathrm{mix\text{-}w}}$, heat flux to LOX ($q_{\mathrm{rad}}^{\mathrm{w\text{-}lox}}$, $q_{\mathrm{con}}^{\mathrm{w\text{-}lox}}$), and radiative heat flux q_{rad}^{w}. The temperature of LOX is determined by the heat flux from the wall, vapor–gas mixture in the tank and heat of vaporization of LOX.

The key heat fluxes that determine the vaporization process of LOX are now considered. The radiant heat flux from the vapor–gas mixture to the LOX surface is

$$q_{\mathrm{rad}}^{\mathrm{mix\text{-}lox}} = \sigma \epsilon_{\mathrm{mix}} F_{\mathrm{lox}} \left(T_{\mathrm{mix}}^4 - T_{\mathrm{lox}}^4\right), \tag{20}$$

where the area of the surface of vaporization of LOX, F_{lox}, depends on the mechanical condition in the tank. If LOX is accumulated at the bottom of the tank, then F_{lox} equals the cross section area of the tank. If the liquid oxygen is in the drop state, then F_{lox} is the total surface of all the drops. The convective heat flux from the vapor–gas mixture to the oxygen surface is

$$q_{\mathrm{con}}^{\mathrm{mix\text{-}lox}} = \alpha_{\mathrm{mix}} F_{\mathrm{lox}} \left(T_{\mathrm{mix}} - T_{\mathrm{lox}}\right), \tag{21}$$

with

$$\alpha_{\mathrm{mix}} = \frac{\lambda_{\mathrm{mix}} Nu_{\mathrm{mix}}}{l} \tag{22}$$

being the heat-exchange coefficient of the vapor–gas mixture to the surface of evaporation of the oxygen in the tank, and where λ_{mix} is the thermal conductivity of the vapor–gas mixture in the tank, and l is the characteristic dimension that is equal to the diameter of the oxygen tank. α_{mix} depends also on the Nusselt number Nu_{mix}, which is determined by the vaporization type of LOX: evaporation from the free surface, nucleate boiling or film boiling. q_{con} and q_{rad}, among other contributors to the heat exchange process, are defined similarly to Eqs. (21) and (22).

If free surface vaporization is the dominant vaporization mechanism, the Nusselt number can be expressed as [88]

$$Nu_{\mathrm{ev}} = C_1 Re_{\mathrm{ev}}^{0.8} Pr_{\mathrm{ev}}^{0.43} \tag{23}$$

where Re_{ev} is the Reynolds number, Pr_{ev} is the Prandtl number for the vapor–gas mixture, and C_1 is equal to 0.037.

In the case of nucleate boiling, the Nusselt number becomes [88]

$$Nu_{\mathrm{nuc}} = \frac{\alpha d_0}{\lambda} = 75(Pe \cdot Fo)^{0.7} Pr^{-0.2}. \tag{24}$$

For the nucleate boiling case, the characteristic dimension is the average diameter of the bubble departure diameter d_0, that can be considered independent on the heat flux q. Consequently, the Peclet number for heat exchange during nucleate boiling is

$$Pe = \frac{q d_0}{r_* \rho_v a}, \tag{25}$$

with an average diameter of the bubble departure diameter defined by Fritz's equation [89]

$$d_0 = 1.2\theta \sqrt{\frac{\sigma}{g(\rho_l - \rho_v)}}, \tag{26}$$

where θ is the contact angle in rad, g is the inertial acceleration, ρ_l and ρ_v are the densities of the liquid and gas oxygen, q is the heat flux density, r_* is the specific heat of evaporation, and a is the temperature conductivity coefficient. The Fourier number for the nucleate boiling of oxygen is

$$Fo = \frac{a}{d_0^2 f}, \tag{27}$$

with

$$f\sqrt{d_0} = 0.56 \left(\frac{\rho_l - \rho_v}{\rho_v} g\right)^{1/2} \tag{28}$$

being the frequency of formation of the vapor bubbles.

Finally, in a film boiling scenario with a large liquid volume on vertical surfaces as well as on horizontal cylinders and spheres, it is recommended to use the similarity equation

$$Nu_f = 0.18 Ra^{1/3}, \tag{29}$$

where

$$Ra = \frac{g l_0^3}{\nu_v a_v} \frac{\rho_l - \rho_v}{\rho_v} \tag{30}$$

is the Rayleigh number that characterizes the behavior of a fluid with a temperature gradient, and where

$$l_0 = \frac{\sigma}{g(\rho_l - \rho_v)} \tag{31}$$

is the capillarity constant, selected as a characteristic length.

Table 5
Mass from different components required for the flip around and settling maneuvers in the first and second stages.

System	Flip around		Settling	
	1st	2nd	1st	2nd
Time [s]	9.7	5.2	40.3	12.5
Gas, nozzles [kg]	22.9	6.14	305	94.6
Vaporized O_2 [kg]	53.9	15	304	92
PGS [kg]	40	40	–	–
Catalyst [kg]	0.5	0.5	–	–
H_2O_2 balloon [kg]	4.6	1.24	5.8	1.77
H_2O_2 [kg]	42	11.4	53	16.2
Helium [kg]	0.069	0.02	0.668	0.2

4.5. Performance analysis

The alternate PGS mode, that reduces the average tank temperature in comparison with a standalone PGS operation, is employed in the analysis. A combined operation with the tank pressurization system reduces oxygen evaporation and preserves it for the operation of the LRE. The ratio of hydrogen peroxide and helium mass flow is not optimized in the results presented in this work, where one of the possible combinations was chosen. However, even this sub-optimal set point reflects the efficiency of the alternate operation of the PGS and helium pressurization systems.

Fig. 12 shows the time evolution of different variables of the PGS for the nozzle thrust values reported in Table 4. After stage separation, the supply of hydrogen peroxide to the LOX tank leads to an operating pressure of ∼4 atm in the oxygen tank. Fig. 12(b) shows the time evolution of this variable. During the first six seconds after separation of the stage and supply of heat to the tank, the pressure increases from 2.7 to 4 atm. As noted above, the given pressure level in the tank is maintained by the joint operation of the PGS and the supply of helium to the LOX tank, that are set manually and may be optimized in future works. From 9 to 95 s, the stage performs the flip-around and propellant settling maneuvers as described in Fig. 9. Fig. 12(a) shows the mass flow rates of hydrogen peroxide, helium, gas through jet nozzles, and vaporized oxygen during this process. Fig. 12(d) depicts the temperature of the oxygen tank, that increases up to 275 K without violating the standard thermal stability limits of 300–350 K.

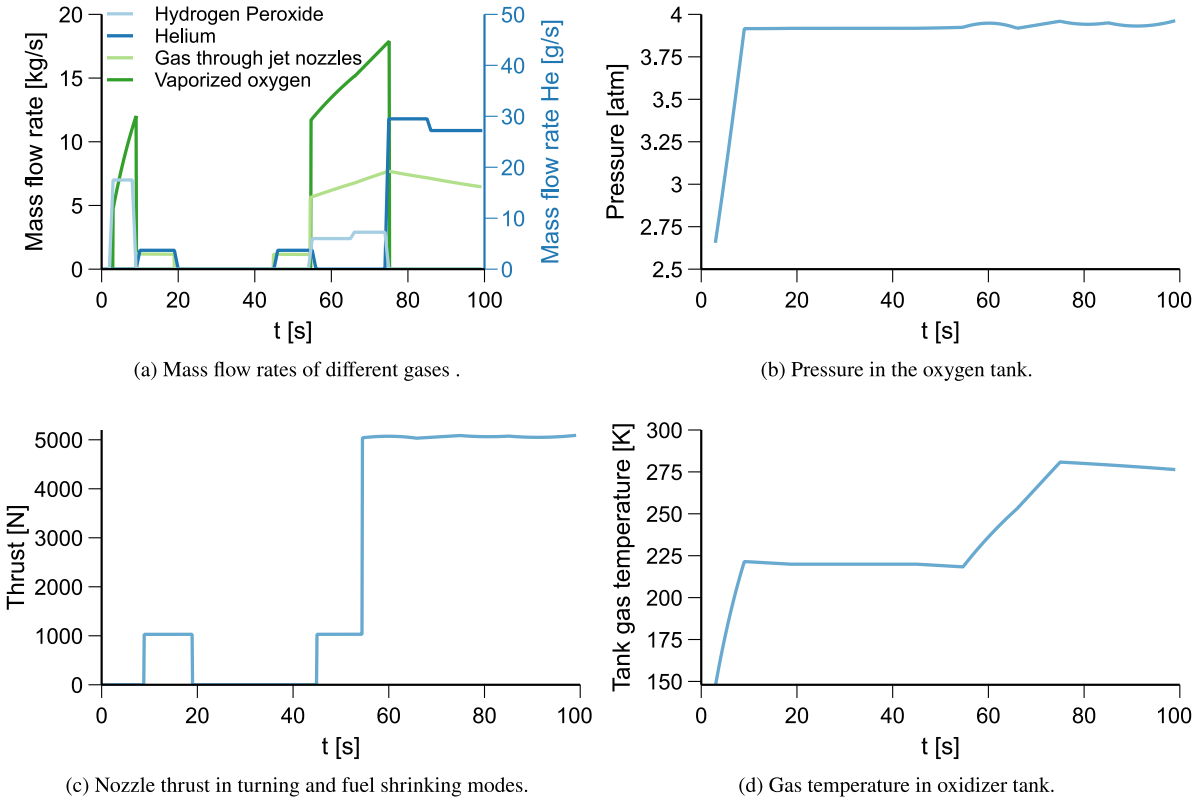

(a) Mass flow rates of different gases .

(b) Pressure in the oxygen tank.

(c) Nozzle thrust in turning and fuel shrinking modes.

(d) Gas temperature in oxidizer tank.

Fig. 12. Performance of the PGS.

Table 5 shows the results of the flip around and propellant settling maneuvers separately. A total of 327.9 kg of gas are employed by the nozzles during the operation of the PGS, with 354 kg of oxygen, 95 kg of hydrogen peroxide, and 0.7 kg of helium being consumed. After the PGS operation, the gas residuals (composed of vaporized oxygen, water vapor, and helium) are needed to maintain the tank pressure of 4 atm as a working body for the gas thrusters, that are in charge of stage orientation and stabilization during the flight. The PGS mass budget of 40 kg includes the gas generator (5 kg), nozzles (10 kg), valves, pipes and other hardware components. The total mass of the nozzles depends on the selected configuration: 8 nozzles are arbitrarily selected in this work, with 2 of them having a higher thrust. The mass values are strongly dependent on the technical decisions of the designers, who will have their own constraints and engineering vision of the PGS, including the length of the pipes, number of valves, etc. Active catalysts (e.g. potassium permanganate grains, silver mesh, copper, or other metals [90]) are used for hydrogen peroxide decomposition. The catalyst does not lose its properties when exposed to the low temperature of the cryogenic tank or the high temperatures of the combustion reaction. The temperature of the hydrogen peroxide decomposition products can be controlled by tuning the hydrogen peroxide concentration [91], which allows the mass evaporation rate to be modified when the PGS is used in combination with the pressurizer gas helium.

In order to minimize propellant residuals in the gas phase at the moment of PGS operation termination, it is necessary to optimize the helium and hydrogen peroxide input cyclogram (e.g. using the Pontryagin maximum principle or dynamic programming [92]). An optimum flow rate combination reduces the residual gas both in the balloons and in the tank after vaporization, and also the final PGS mass.

5. Hybrid magnetic gasification

The PGS is faster and more controllable than the magnetic approaches discussed in Section 3, but involves a higher mass penalty and

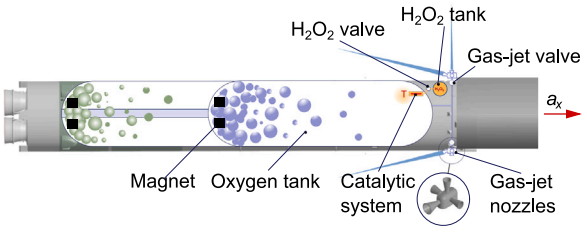

Fig. 13. Hybrid Propellant Gasification System.

complexity. A combination of the MP^2 and PGS technologies can potentially enhance the robustness and performance of the overall propellant settling system. This hybrid approach, depicted in Fig. 13, involves a permanent magnet located at the fuel outlet and a smaller PGS aimed at carrying out the flip-around phase and the shorter propellant settling maneuver described in Fig. 14. The initial acceleration induced on the liquid residuals during the settling phase starts a slow movement toward the bottom of the tank, where the magnetic force is stronger and thus able to efficiently collect the liquid droplets.

Fig. 15 depicts the time required by an LOX droplet to reach the bottom of the tank when subject to the magnetic field generated by a 10^4 At magnet as a function of its initial velocity and distance to the tank outlet. Based on Table 3, such magnet has a mass of ~5.2 kg. The results are computed from a modified version of Eq. (10), and prove that an initial inertial kick can significantly extend the reach of the MP^2 system. Initial droplet velocities of just 5 to 10 mm/s allow the magnet to collect the necessary residual propellant mass under all engine restart configurations listed in Table 2 for both stages assuming that the droplets are uniformly distributed in the tank volume. The 5 kN PGS nozzles, that induce accelerations of ~0.23 m/s^2 in the first stage, would theoretically need to operate for less than 0.05 s to induce these droplet velocities, reducing the propellant settling window in

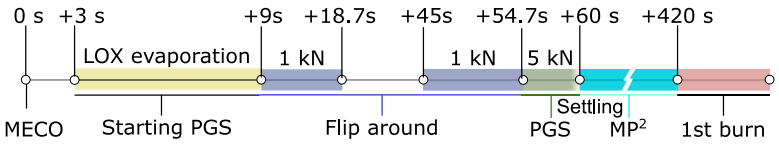

Fig. 14. Hybrid PGS operation cycle for the first stage.

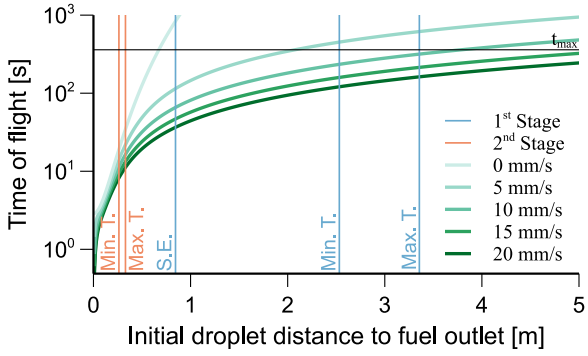

Fig. 15. Time required by a LOX droplet to reach the bottom of the tank as a function of its initial position and velocity when subject to a 10^4 At coil located at the tank outlet. The minimum tank settling length required by the single engine (S.E.), minimum thrust (Min. T.) and maximum thrust (Max. T.) configurations is superposed.

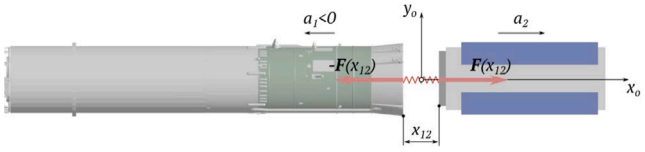

Fig. 16. Stage separation model.

about 40 s. The operation of the nozzles would need to be extended to account for transient effects and fluid–structure interactions, but this would only increase the effectivity of the system. Based on Table 5, the associated PGS mass savings would be close to 90 kg and 53 kg in the first and second stages, respectively, resulting in total hybrid system masses of 93 and 58 kg. The gas generated during the turn around phase is considered in this estimation.

If PGS and MP^2 are used simultaneously, there is a risk of liquid carry-over when the droplets held by the magnet are pushed by the gas flow. To prevent this effect, the velocity of the gas near the liquid must be below the critical value V_{cr}, derived as [93]

$$V_{cr} = \sqrt{\frac{\rho_l + \rho_g}{\rho_l}} \sqrt[4]{\frac{4 n_x g \sigma (\rho_l - \rho_g)}{\rho_g^2}} \tag{32}$$

where n_x is the overload, or ratio of the absolute value of the linear acceleration caused by non-gravitational forces to the standard free-fall acceleration at the Earth's surface. As shown in Eq. (32), the overload determines the critical velocity.

Early studies have been conducted to estimate the gas velocity induced by the PGS in the propellant tank of a Soyuz-2-like launch vehicle, showing that the flow is slowed down to 15 m/s at the bottom of the container with an input velocity of 500 m/s [94]. The initial gas velocity is set to 25 m/s in this work, which results in a negligible gas movement near the tank outlet. The initial gas velocity is, among other properties like the flow direction, a relatively flexible design parameter that must be set during the development of the system. An additional aspect to note is that the overload equals 0 when the rocket engines are turned off and increases slightly when the PGS is operative. If the residual gas movement reaches the critical value for low overload values, then the liquid droplets near the magnet may be disrupted.

6. Summary and conclusions

Five novel cryogenic propellant settling approaches have been explored in this work: passive magnetic retention, magnetic recovery, magnetic traps, propellant gasification, and hybrid magnetic gasification. The advantages and disadvantages of each of them have been discussed, and preliminary mass budgets have been derived. Table 6 summarizes the main results from the analysis presented in previous sections.

While the passive magnetic retention strategy exceeds any reasonable mass budget, the magnetic trap approach can potentially reduce the mass of existing propellant settling systems by one to two orders of magnitude, leading to more than half a million dollar savings per launch and stage. This comes at the cost of higher complexity and modeling efforts, particularly in the fuel tank. Although less efficient, the magnetic recovery system also seems competitive with respect to current technologies. Because this approach depends on the availability of uniformly distributed free-floating propellant droplets, fluid–structure interactions may undermine its performance. The PGS, which represents a relatively more conventional approximation to the problem, can also lead to moderate mass savings that are significantly increased when operated in combination with a magnetic retention system. As with any other low-TRL technology, numerous technical challenges remain that can only be addressed with a more detailed numerical and experimental analysis.

Ullage engines have been employed since the beginning of the space era and are nowadays regarded as a robust active settling solution. However, publicly available data indicates that they also involve significant mass and economic penalties that may be reduced with novel approaches. Such approaches face additional challenges when dealing with cryogenic propellants and must demonstrate the same level of reliability and robustness in order to become competitive. Although the MP^2 and propellant gasification systems introduced in this work are still in a very early stage of development, the analysis here presented offers reasons to persevere in their development.

Declaration of competing interest

The authors declare that they have no known competing financial interests or personal relationships that could have appeared to influence the work reported in this paper.

Acknowledgments

The work was carried out with the support of the grant No. 2019-0251 of the Ministry of Education and Science of the Russian Federation. A.R.C. acknowledges the funding received by the 2021 *Rafael del Pino* Foundation Excellent Fellowship and the *la Caixa* Foundation, Spain (ID 100010434), under agreement LCF/BQ/AA18/11680099.

Appendix. Stage separation model

The accelerations experienced by each stage during separation are modeled after assuming that the process is carried out by spring pushers

Table 6
Comparison of different propellant settling approaches and mass budgets for first and second stages.

	Advantages	Disadvantages	Mass, 1st [kg]	Mass, 2nd [kg]
Passive Magnetic Retention	– Simple – Robust – Thoroughly studied	– Beyond current technological capabilities – Massive unless stage operation is adapted – Limited control	$\to \infty$	>1000
Magnetic Recovery	– Lightweight – Simple	– Sensitive to fluid–structure interactions – Slow – Requires tank outlet redesign – Very low TRL	104	1–10
Magnetic Trap	– Lightweight – Simple – Potentially robust	– Requires careful trap design – Requires tank outlet redesign – Very low TRL	40	6
Propellant Gasification System	– Robust – Provides settling and attitude control – Fast to operate – More traditional design	– Complex – Sensitive to liquid movement – Very low TRL	147	71
Hybrid Magnetic Gasification	– Lightweight – More robust than magnetic recovery – Provides settling and attitude control – Fast to operate – Boosts magnet performance	– Complex – Sensitive to liquid movement – Requires tank outlet redesign – Very low TRL	93	58

with total initial force F_b, final force F_e, and stroke h. Thus, the total force acting on the stage is

$$F(x_{12}) = F_b - cx_{12} \text{ if } x_{12} \leq h, 0 \text{ otherwise}, \tag{33}$$

with $c = (F_b - F_e)/h$ being the total stiffness of the springs, and where the geometrical parameters of the problem are defined in Fig. 16. After applying Newton's second law and solving the resulting differential equation, the duration of the maneuver becomes

$$t_h = \sqrt{\frac{m_{12}}{c}} \arccos \frac{F_e}{F_b}, \tag{34}$$

where $m_{12} = m_1 m_2/(m_1 + m_2)$. The acceleration of the stage with respect to the orbital frame is

$$a_1 = -\frac{F_b}{m_1} \cos \sqrt{\frac{c}{m_{12}}} t \text{ if } t \leq t_h, 0 \text{ otherwise}. \tag{35}$$

The values $F_e = 0.3F_b$, and $h = 0.2$ m are adopted in this work, with $F_b = 12.1$ kN and $F_b = 4.5$ kN in the first and second stages, respectively. Empty and total masses are considered for the deployed and remaining stages with a payload mass of 15 t. The resulting propellant dispersion velocities range between 0.45 and 0.5 m/s, a range that seems to agree with observations from SpaceX's CRS-5 mission.

References

[1] Inter-Agency Space Debris Coordination Committee, IACD Space Debris Mitigation Guidelines, Tech. Rep. IADC-02-01, IADC, 2020.

[2] L. Anselmo, C. Pardini, Ranking upper stages in low Earth orbit for active removal, Acta Astronaut. 122 (2016) 19–27, http://dx.doi.org/10.1016/j.actaastro.2016.01.019.

[3] J.C. Liou, An active debris removal parametric study for LEO environment remediation, Adv. Space Res. 47 (11) (2011) 1865–1876, http://dx.doi.org/10.1016/j.asr.2011.02.003.

[4] D. McKnight, R. Witner, F. Letizia, S. Lemmens, L. Anselmo, C. Pardini, A. Rossi, C. Kunstadter, S. Kawamoto, V. Aslanov, J.-C. Dolado Perez, V. Ruch, H. Lewis, M. Nicolls, L. Jing, S. Dan, W. Dongfang, A. Baranov, D. Grishko, Identifying the 50 statistically-most-concerning derelict objects in LEO, Acta Astronaut. 181 (2021) 282–291, http://dx.doi.org/10.1016/j.actaastro.2021.01.021.

[5] V. Trushlyakov, Y. Shatrov, Improving of technical characteristics of launch vehicles with liquid rocket engines using active onboard de-orbiting systems, Acta Astronaut. 138 (2017) 19–27, http://dx.doi.org/10.1016/j.actaastro.2017.05.018.

[6] S. Lednev, T. Koroleva, P. Krechetov, A. Sharapova, I. Semenkov, A. Karpachevskiy, Revegetation of areas disturbed by rocket impact in Central Kazakhstan, Ecoscience 25 (1) (2018) 25–38, http://dx.doi.org/10.1080/11956860.2017.1396100.

[7] T.V. Koroleva, P.P. Krechetov, I.N. Semenkov, A.V. Sharapova, S.A. Lednev, A.M. Karpachevskiy, A.D. Kondratyev, N.S. Kasimov, The environmental impact of space transport, Transp. Res. D 58 (2018) 54–69, http://dx.doi.org/10.1016/j.trd.2017.10.013.

[8] R.P. Patera, K.R. Bohman, M.A. Landa, C.D. Pao, R.T. Urbano, M.D. Weaver, D.C. White, DMSP-17 Upper Stage Controlled Reentry Disposal, Tech. Rep. ATR-2007(8083)-1, The Aerospace Corporation, 2006.

[9] V.I. Trushlyakov, V.V. Shalay, Y.T. Shatrov, Reduction of the Technogenic Impact of Launch Vehicles on the Liquid Toxic Components of Rocket Fuel on the Environment, Tech. rep., Omsk State Technical University, 2004, p. 2019.

[10] P. Giacalone, Detail design of the surface tension propellant management device for the Intelsat VII communication satellite, in: AIAA 29th Joint Propulsion Conference and Exhibit, 1993, http://dx.doi.org/10.2514/6.1993-1802, AIAA Paper 1993-1802.

[11] r. Jaekle, Propellant management device conceptual design and analysis - Traps and troughs, in: 31st Joint Propulsion Conference and Exhibit, 1995, http://dx.doi.org/10.2514/6.1995-2531, AIAA Paper 1995-2531.

[12] W. Tam, M. Drey, J. D. Jaeckle, L. Larsson, Design and manufacture of an oxidizer tank assembly, in: 37th Joint Propulsion Conference and Exhibit, 2001, http://dx.doi.org/10.2514/6.2001-3825, AIAA Paper 2001-3825.

[13] P. Behruzi, Concept analysis of PMD designs for future upper stages, in: 54th International Astronautical Congress of the International Astronautical Federation, the International Academy of Astronautics, and the International Institute of Space Law, 2003, http://dx.doi.org/10.2514/6.IAC-03-S.1.07.

[14] P. Behruzi, M. Michaelis, Development of a propellant management device (PMD) for restartable future cryogenic upper stages, in: 42nd AIAA/ASME/SAE/ASEE Joint Propulsion Conference &Amp; Exhibit, 2006, http://dx.doi.org/10.2514/6.2006-5053, AIAA Paper 2006-5053.

[15] G. Burge, J. Blackmon, Study and Design of Cryogenic Propellant Acquisition Systems. Volume 1: Design Studies, Tech. Rep. CR-120300/MDC-G5038-VOL-1, NASA, 1973.

[16] S. Boraas, A.J. LaBruna, In-space propellant acquisition with pleated screen tubes, J. Spacecr. Rockets 13 (6) (1976) 377–384, http://dx.doi.org/10.2514/3.57101.

[17] J.W. Hartwig, Propellant management devices for low-gravity fluid management: Past, present, and future applications, J. Spacecr. Rockets 54 (4) (2017) 808–824, http://dx.doi.org/10.2514/1.A33750.

[18] S.R. Darr, C.F. Camarotti, J.W. Hartwig, J.N. Chung, Hydrodynamic model of screen channel liquid acquisition devices for in-space cryogenic propellant management, Phys. Fluids 29 (1) (2017) 017101, http://dx.doi.org/10.1063/1.4973671.

[19] G.K. Platt, Space Vehicle Low Gravity Fluid Mechanics Problems and the Feasibility of Their Experimental Investigation, Tech. Rep. TM X-53589, NASA, 1967, URL https://ntrs.nasa.gov/citations/19670031036.

[20] W.L. Browning, S-4B/5 Auxiliary Propulsion System 90-day Recycle Capability Test Report, Module 1, Tech. Rep. DAC-56728, McDonnell Douglas Astronautics Company, 1969, URL https://ntrs.nasa.gov/citations/19700026606.

[21] K. Coates, E. Donald, Investigation of SA-501 S-4B Auxiliary Propulsion System Flight Anomalies, Tech. Rep. TN D-5207, NASA, 1969, URL https://ntrs.nasa.gov/citations/19690016846.

[22] K. Austad, The Common Centaur upper stage, in: 37th Joint Propulsion Conference and Exhibit, 2001, http://dx.doi.org/10.2514/6.2001-3842, AIAA Paper 2001-3842.

[23] Space Exploration Technologies Corporation, Falcon User's Guide, 2021.

[24] P. Anz-Meador, Root cause classification of breakup events 1961–2018, in: First International Orbital Debris Conference, Houston, TX, 2019, URL www.hou.usra.edu/meetings/orbitaldebris2019/orbital2019paper/pdf/6040.pdf.

[25] Saturn Flight Evaluation Working Group, Marshall Space Flight Center, Saturn 5 Launch Vehicle Flight Evaluation Report-AS-511 Apollo 16 Mission, Tech. Rep. TM-X-69535, NASA, 1972, URL https://ntrs.nasa.gov/citations/19730025090.

[26] A.P. Adzhan, E.L. Akim, O.M. Alifanov, Rocket and space technology, Eng. Encycl. 4 (2012) 925.

[27] H. Jones, The recent large reduction in space launch cost, in: 48th International Conference on Environmental Systems, Albuquerque, NM, 2018, URL hdl.handle.net/2346/74082.

[28] Á. Romero-Calvo, F. Maggi, H. Schaub, Magnetic positive positioning: Toward the application in space propulsion, Acta Astronaut. 187 (2021) 348–361, http://dx.doi.org/10.1016/j.actaastro.2021.06.045, URL https://www.sciencedirect.com/science/article/pii/S0094576521003428.

[29] V.I. Trushlyakov, V.A. Urbansky, V.V. Yudintsev, Reducing environmental damage after emergency engine cutoff of the launch vehicle, J. Spacecr. Rockets 58 (3) (2021) 685–696, http://dx.doi.org/10.2514/1.A34912.

[30] G. Sutton, O. Biblarz, Rocket Propulsion Elements, eighth ed., John Wiley & Sons, 2010.

[31] A.P. Vasilev, V.M. Kudryavtsev, V.A. Kuznetsov, V.D. Kurpatenkov, A.M. Obelnitskii, Fundamentals of the Theory and Calculation of Liquid Propellant Rocket Engines, Vol. 2, fourth ed., Kudryavtsev M.V., 1993, p. 281.

[32] C. Roland, J.R. Grace, M.E. Weber, Bubbles, Drops and Particles, Academic Press, 1978.

[33] J.C. Boulware, H. Ban, S. Jensen, S. Wassom, Experimental studies of the pressures generated by a liquid oxygen slug in a magnetic field, J. Magn. Magn. Mater. 322 (13) (2010) 1752–1757, http://dx.doi.org/10.1016/j.jmmm.2009.12.022.

[34] K. Kinefuchi, H. Kobayashi, Theoretical and experimental study of the active control of bubble point pressure using a magnetic field and its applications, Phys. Fluids 30 (6) (2018) 062101, http://dx.doi.org/10.1063/1.5034222.

[35] A. Causevica, P. Sahli, F. Hild, K. Grunwald, M. Ehresmann, G. Herdrich, PAPELL: Interaction study of ferrofluid with electromagnets of an experiment on the international space station, in: Proceedings of the 69th International Astronautical Congress, 2018, pp. 1–5.

[36] Á. Romero-Calvo, Ö. Akay, H. Schaub, K. Brinkert, Magnetic phase separation in microgravity, npj Microgravity 8 (1) (2022) 32, http://dx.doi.org/10.1038/s41526-022-00212-9.

[37] D. Ludovisi, S.S. Cha, N. Ramachandran, W.M. Worek, Heat transfer of thermocapillary convection in a two-layered fluid system under the influence of magnetic field, Acta Astronaut. 64 (11) (2009) 1066–1079, http://dx.doi.org/10.1016/j.actaastro.2009.01.018.

[38] A. Bozhko, G. Putin, Thermomagnetic convection as a tool for heat and mass transfer control in nanosize materials under microgravity conditions, Microgravity Sci. Technol. 21 (1) (2009) 89–93, http://dx.doi.org/10.1007/s12217-008-9059-7.

[39] B.A. Jackson, K.J. Terhune, L.B. King, Ionic liquid ferrofluid interface deformation and spray onset under electric and magnetic stresses, Phys. Fluids 29 (6) (2017) 064105, http://dx.doi.org/10.1063/1.4985141.

[40] K. Lemmer, Propulsion for CubeSats, Acta Astronaut. 134 (2017) 231–243, http://dx.doi.org/10.1016/j.actaastro.2017.01.048.

[41] R.E. Rosensweig, Ferrohydrodynamics, Dover Publications, 1997.

[42] Á. Romero-Calvo, G. Cano-Gómez, T.H. Hermans, L. Parrilla Benítez, M. Herrada, E. Castro-Hernández, Total magnetic force on a ferrofluid droplet in microgravity, Exp. Therm Fluid Sci. 117 (2020) 110124, http://dx.doi.org/10.1016/j.expthermflusci.2020.110124.

[43] S. Papell, Low viscosity magnetic fluid obtained by the colloidal suspension of magnetic particles, 1963, US Patent 3215572.

[44] J. Martin, J. Holt, Magnetically Actuated Propellant Orientation Experiment, Controlling fluid Motion With Magnetic Fields in a Low-Gravity Environment, Tech. Rep. TM-2000-210129, NASA, 2000.

[45] D.R. Lide, CRC Handbook of Chemistry and Physics: 84th Edition, CRC Press, 2003.

[46] J. Hochstein, R. Warren Jr., J. George Schmidt, J. Hochstein, R. Warren Jr., J. George Schmidt, Magnetically actuated propellant orientation (MAPO) experiment - Pre-flight flow field predictions, in: Proceedings of the 35th Aerospace Sciences Meeting and Exhibit, 1997, pp. 1–11, http://dx.doi.org/10.2514/6.1997-570, AIAA Paper 1997-570.

[47] J. Marchetta, J. Hochstein, Fluid capture by a permanent ring magnet in reduced gravity, in: Proceedings of the 37th Aerospace Sciences Meeting and Exhibit, Reno, NV, USA, 1999, pp. 1–14, http://dx.doi.org/10.2514/6.1999-845, AIAA Paper 1999-845.

[48] J. Marchetta, J. Hochstein, Simulation and dimensionless modeling of magnetically induced reorientation, in: Proceedings of the 38th Aerospace Sciences Meeting and Exhibit, Renno, NV, USA, 2000, pp. 1–13, http://dx.doi.org/10.2514/6.2000-700, AIAA Paper 2000-700.

[49] J. Marchetta, J. Hochstein, D. Sauter, B. Simmons, Modeling and prediction of magnetic storage and reorientation of LOX in reduced gravity, in: 40th AIAA Aerospace Sciences Meeting & Exhibit, 2002, pp. 1–19, http://dx.doi.org/10.2514/6.2002-1005, AIAA Paper 2002-1005.

[50] J.G. Marchetta, Simulation of LOX reorientation using magnetic positive positioning, Microgravity - Sci. Technol. 18 (1) (2006) 31, http://dx.doi.org/10.1007/BF02908417.

[51] J. Marchetta, K. Roos, A three-dimensional computational simulation of magnetic positive positioning, in: 45th AIAA Aerospace Sciences Meeting and Exhibit, 2007, pp. 1–11, http://dx.doi.org/10.2514/6.2007-956, AIAA Paper 2007-956.

[52] J. Marchetta, K. Roos, Simulating magnetic positive positioning of liquids in a transient acceleration field, in: 46th AIAA Aerospace Sciences Meeting and Exhibit, 2008, pp. 1–11, http://dx.doi.org/10.2514/6.2008-820, AIAA Paper 2008-820.

[53] J.G. Marchetta, B.D. Simmons, J.I. Hochstein, Magnetic retention of LO2 in an accelerating environment, Acta Astronaut. 62 (8) (2008) 478–490, http://dx.doi.org/10.1016/j.actaastro.2008.01.016.

[54] J. Marchetta, A. Winter, Simulation of magnetic positive positioning for space based fluid management systems, Math. Comput. Modelling 51 (9) (2010) 1202–1212, http://dx.doi.org/10.1016/j.mcm.2010.01.002.

[55] Á. Romero-Calvo, T.H. Hermans, G.C. Gómez, L.P. Benítez, M.H. Gutiérrez, E. Castro-Hernández, Ferrofluid dynamics in microgravity conditions, in: Proceedings of the 2nd Symposion on Space Educational Activities, Budapest, Hungary, 2018, pp. 1–5.

[56] Á. Romero-Calvo, G. Cano Gómez, E. Castro-Hernández, F. Maggi, Free and forced oscillations of magnetic liquids under low-gravity conditions, J. Appl. Mech. 87 (2) (2020) 021010, http://dx.doi.org/10.1115/1.4045620.

[57] Á. Romero-Calvo, A. García-Salcedo, F. Garrone, I. Rivoalen, G. Cano-Gómez, E. Castro-Hernández, M.H. Gutiérrez, F. Maggi, StELIUM: A student experiment to investigate the sloshing of magnetic liquids in microgravity, Acta Astronaut. 173 (2020) 344–355, http://dx.doi.org/10.1016/j.actaastro.2020.04.013.

[58] Á. Romero-Calvo, M.Á. Herrada, T.H. Hermans, L. P. Benítez, G. Cano-Gómez, E. Castro-Hernández, Axisymmetric ferrofluid oscillations in a cylindrical tank in microgravity, Microgravity Sci. Technol. 33 (50) (2021) http://dx.doi.org/10.1007/s12217-021-09894-4.

[59] Á. Romero-Calvo, F. Garrone, A. García-Salcedo, I. Rivoalen, G. Cano-Gómez, E. Castro-Hernández, F. Maggi, Free surface reconstruction of opaque liquids in microgravity. Part 2: Drop tower campaign, Acta Astronaut. 189 (2021) 269–277, http://dx.doi.org/10.1016/j.actaastro.2021.07.020.

[60] Á. Romero-Calvo, A. García-Salcedo, F. Garrone, I. Rivoalen, F. Maggi, Lateral and axisymmetric ferrofluid oscillations in a cylindrical tank in microgravity, AIAA J. (2022) in press.

[61] A. Myshkis, R. Wadhwa, Low-Gravity Fluid Mechanics: Mathematical Theory of Capillary Phenomena, Springer, 1987.

[62] B. Pugh, D. Kramer, C. Chen, Demagnetizing factors for various geometries precisely determined using 3-D electromagnetic field simulation, IEEE Trans. Magn. 47 (10) (2011) 4100–4103, http://dx.doi.org/10.1109/TMAG.2011.2157994.

[63] Á. Romero-Calvo, G. Cano-Gómez, H. Schaub, Diamagnetically enhanced electrolysis and phase separation in low gravity, AIAA J. Spacecr. Rockets (2021) 1–13, http://dx.doi.org/10.2514/1.A35021, in press.

[64] J. Campbell, E. Eldridge, J. Thompson, Handbook on Materials for Superconducting Machinery, Tech. Rep. MCIC-HB-04, ARPA, 1974.

[65] A. Trench, J.P. Sykes, Rare earth permanent magnets and their place in the future economy, Engineering 6 (2) (2020) 115–118, http://dx.doi.org/10.1016/j.eng.2019.12.007.

[66] K. Halbach, Design of permanent multipole magnets with oriented rare earth cobalt material, Nucl. Instrum. Methods 169 (1) (1980) 1–10, http://dx.doi.org/10.1016/0029-554X(80)90094-4.

[67] S.R. Trout, S. Constantinides, Using Permanent Magnets at Low Temperature, Tech. Rep. TN 0302, Arnold Magnetic Technologies, 2021, URL www.arnoldmagnetics.com/wp-content/uploads/2017/10/TN_0302_rev_150715.pdf.

[68] K. Uestuener, M. Katter, R. Blank, D. Benedikt, J. Bahrdt, A. Gaupp, B. Klemke, F. Grüner, R. Weingartner, Sintered (Pr,Nd)-Fe-B permanent magnets with $(BH)_{max}$ of 520.kJ/m^3 at 85 k for cryogenic applications, in: 20th International Workshop on Rare-Earth and Future Permanent Magnets and their Applications, 2008.

[69] J.-C. Huang, H. Kitamura, C.-S. Yang, C.-K. Yang, S. Mizumoto, C.-H. Chang, C.-H. Chang, C.-S. Hwang, Development of cryogenic permanent magnet undulators at NSRRC, AIP Conf. Proc. 2054 (1) (2019) 030022, http://dx.doi.org/10.1063/1.5084585.

[70] K. Tsuchiya, X. Wang, S. Fujita, A. Ichinose, K. Yamada, A. Terashima, A. Kikuchi, Superconducting properties of commercial REBCO-coated conductors with artificial pinning centers, Supercond. Sci. Technol. 34 (2021) 105005, http://dx.doi.org/10.1088/1361-6668/ac1e65.

[71] W. Fietz, R. Heller, S. Schlachter, W. Goldacker, Application of high temperature superconductors for fusion, Fusion Eng. Des. 86 (6) (2011) 1365–1368, http://dx.doi.org/10.1016/j.fusengdes.2010.11.018, Proceedings of the 26th Symposium of Fusion Technology (SOFT-26).

[72] H. Weijers, W. Markiewicz, D. Abraimov, H. Bai, D. Hilton, A. Gavrilin, D. Larbalestier, J. Lu, T.P. Murphy, P. Noyes, A.J. Voran, NHMFL, Testing of prototype coils for the NHMFL 32 T superconducting user magnet, in: Applied Superconductivity Conference, Charlotte, NC, 2014.

[73] O.P. Ivakhnenko, D.K. Potter, Magnetic susceptibility of petroleum reservoir fluids, Phys. Chem. Earth Parts A/B/C 29 (13) (2004) 899–907, http://dx.doi.org/10.1016/j.pce.2004.06.001, Paleo, Rock and Environmental Magnetism.

[74] P.R. Choudhury, Slurry fuels, Prog. Energy Combust. Sci. 18 (5) (1992) 409–427, http://dx.doi.org/10.1016/0360-1285(92)90008-O.

[75] C.-Y. Hong, I.J. Jang, H.E. Horng, C.J. Hsu, Y.D. Yao, H.C. Yang, Ordered structures in Fe3O4 kerosene-based ferrofluids, J. Appl. Phys. 81 (8) (1997) 4275–4277, http://dx.doi.org/10.1063/1.364800.

[76] E. Ghasemi, A. Mirhabibi, M. Edrissi, R. Aghababazadeh, R.M. Brydson, Study on the magnetorheological properties of maghemite-kerosene ferrofluid, J. Nanosci. Nanotechnol. 9 (7) (2009) 4273–4278, http://dx.doi.org/10.1166/jnn.2009.M45.

[77] V.I. Zubko, Y.I. Dikanskii, D.V. Zubko, S.A. Kunikin, G.I. Sitsko, Electrical and magnetic properties of a kerosene-based magnetic fluid subjected to the action of electric and magnetic fields, J. Eng. Phys. Thermophys. 91 (3) (2018) 806–811, http://dx.doi.org/10.1007/s10891-018-1803-2.

[78] D. Susan-Resiga, I. Malaescu, O. Marinica, C. Marin, Magnetorheological properties of a kerosene-based ferrofluid with magnetite particles hydrophobized in the absence of the dispersion medium, Physica B 587 (2020) 412150, http://dx.doi.org/10.1016/j.physb.2020.412150.

[79] L. Maldonado-Camargo, M. Unni, C. Rinaldi, Magnetic characterization of iron oxide nanoparticles for biomedical applications, in: Methods in Molecular Biology (Clifton, N.J.), Vol. 1570, 2017, pp. 47–71, http://dx.doi.org/10.1007/978-1-4939-6840-4_4.

[80] M.L. Voloshin, S.A. Kuda, A.I. Logvinenko, A.N. Mashchenko, E.I. Shevtsov, Experience of development and use of generator pressurization system for tanks of launch vehicles on high-temperature propellants, Space Technol. Missile Armaments 1 (2019) 45–53, http://dx.doi.org/10.33136/stma2019.01.045.

[81] V. Trushlyakov, V. Shalay, J. Shatrov, M. Jakovlev, A. Kostantino, Active de-orbiting onboard system from LEO of upper stages of launchers, in: 5th European Conference on Space Debris, Darmstadt, 2009.

[82] E. Yutkin, V. Trushlyakov, F. Maggi, L. Galfetti, L.T. De Luca, Active onboard deorbiting system for the second stage of Cosmos 3M: a preliminary study, in: 4th European Conference for Aerospace Sciences (EUCASS), 2011, pp. 1–9.

[83] F. Maggi, L. Galfetti, L. De Luca, V.I. Trushlyakov, V.Y. Kudentsov, D.B. Lempert, Thermochemical considerations in support of ADOS propulsion, in: Space Debris Mitigation Workshop, 2010, p. Presentation.

[84] V.I. Trushlyakov, D.B. Lempert, M.E. Bel'kova, Possibility of using gas-generating compositions for increasing the rocket propulsion efficiency, Combust. Explos. Shock Waves 51 (3) (2015) 326–332.

[85] V.I. Trushlyakov, V.A. Urbansky, N.V. Pustovoy, Study of the unusable liquid propellant residues evaporation processes parameters in the tanks of the launch vehicle expended stage in microgravity, J. Phys. Conf. Ser. 1441 (2020) 012121, http://dx.doi.org/10.1088/1742-6596/1441/1/012121.

[86] Arianespace, Soyuz User's Manual, 2012, Issue 2, Revision 0.

[87] G. Dussollier, A. Teissier, Ariane 5 main stage oxygen tank pressurization, in: 29th Joint Propulsion Conference and Exhibit, AIAA-93-1969, Monterey, CA, Monterey, CA, 1993, pp. 1–10, http://dx.doi.org/10.2514/6.1993-1969.

[88] S.S. Kutateladze, Fundamentals of Heat Transfer, Academic Press, New York, 1964.

[89] K. Stephan, Physical fundamentals of vapor bubble formation, in: Heat Transfer in Condensation and Boiling, Springer-Verlag, Berlin, Heidelberg, 1992, pp. 126–139, http://dx.doi.org/10.1007/978-3-642-52457-8_10, Ch. 10.

[90] S.L. Guseinov, S. Fedorov, V. Kosykh, P. Storozhenko, Hydrogen peroxide decomposition catalysts used in rocket engines, Russ. J. Appl. Chem. 93 (2020) 467–487, http://dx.doi.org/10.1134/S1070427220040011.

[91] C. Schumb, C. Satterfield, R. Wentworth, Hydrogen peroxide monograph, J. Am. Pharm. Assoc. (Sci. Ed.) 45 (2) (1956) 128, http://dx.doi.org/10.1002/jps.3030450224.

[92] I.M. Ross, A Primer on Pontryagin's Principle in Optimal Control, Collegiate publishers, 2015.

[93] S.S. Kutateladze, Y.L. Sorokin, On the hydrodynamic stability of some gas-liquid systems, in: Issues of Heat Transfer and Hydraulics of Two-Phase Media, 1961, pp. 315–324.

[94] V. Kudentsov, V. Trushlyakov, Simulation of gas-dynamic flows inside typical rocket fuel tank structures, Bull. Sib. State Automob. Road Acad. 5 (33) (2013) 116–122.